Development of a hepatic cryoinjury model to study liver regeneration

Marcos Sande-Melon[1,2,*], David Bergemann[3,4,*], Juan Manuel González-Rosa[3,4,5#], Andrew Cox[1,2,6,#]

[1] Peter MacCallum Cancer Centre, Melbourne, Victoria, 3000, Australia.
[2] The Sir Peter MacCallum Department of Oncology, The University of Melbourne, Melbourne, Victoria, 3000, Australia.
[3] Cardiovascular Research Centre, Massachusetts General Hospital Research Institute, Charlestown Navy Yard Campus, 149, 13th Street, 02129 MA, USA.
[4] Harvard Medical School.
[5] Biology Department, Morrissey College of Arts and Sciences, Boston College, Chestnut Hill, MA 02467.
[6] Department of Biochemistry and Pharmacology, The University of Melbourne, Melbourne, Victoria, 3000, Australia.
[*] Co-first authors
[#] Co-corresponding authors

jgonzalezrosa@mgh.harvard.edu
andrew.cox@petermac.org

Abstract

The liver is a remarkable organ that can regenerate in response to injury. Depending on the extent of injury, the liver can undergo compensatory hyperplasia or fibrosis. Despite decades of research, the molecular mechanisms underlying these processes are poorly understood. Here, we developed a new model to study liver regeneration based on cryoinjury. To visualise liver regeneration at cellular resolution, we adapted the CUBIC tissue-clearing approach. Hepatic cryoinjury induced a localised necrotic and apoptotic lesion characterised by inflammation and infiltration of innate immune cells. Following this initial phase, we observed fibrosis, which resolved as regeneration re-established homeostasis in 30 days. Importantly, this approach enables the comparison of healthy and injured parenchyma with an individual animal, providing unique advantages to previous models. In summary, the hepatic cryoinjury model provides a fast and reproducible method for studying the cellular and molecular pathways underpinning fibrosis and liver regeneration.

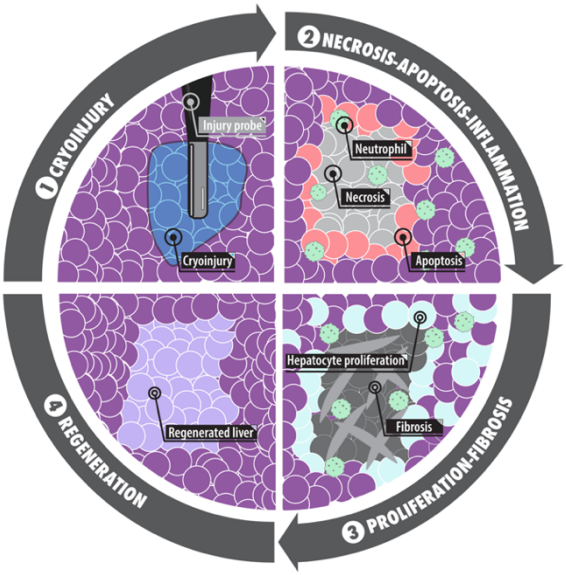

Keywords

Liver regeneration, cryoinjury, inflammation, proliferation, fibrosis, necrosis, apoptosis

Introduction

Regeneration is defined as the anatomical regrowth of an injured organ to restore homeostatic functions. Unlike most human organs, the liver exhibits an unparalleled capacity to regenerate. The process of liver regeneration is multifaceted, as it requires a complex tissue comprised of multiple cell types to sense the extent of the injury and mount an appropriate compensatory regrowth response[1]. Because of this complexity, the molecular underpinnings of liver regeneration are poorly understood.

Chronic liver diseases such as viral infection, alcohol, and non-alcoholic steatohepatitis often exhibit features of a maladaptive response to injury known as fibrosis [2]. The phenomenon of fibrosis is a common wound-healing response in nature in which resident fibroblasts deposit extracellular matrix. In most cases, fibrosis inhibits the regenerative response of organs. However, fibrotic scars can be resolved in zebrafish to enable organ regeneration (e.g., cardiac regeneration following myocardial infarction[3–5]).

Several methods have been used to study liver regeneration in animal models. Among these methods, partial hepatectomy (PHx) is a surgical approach in which a liver lobe is resected, leaving the remnant liver lobes to regenerate[6–8]. In the PHx model of regeneration, there is a limited role for inflammation or fibrosis due to the absence of necrotic regions of tissue. The other dominant methods to study liver regeneration involves exposure to hepatotoxins that induce liver injury and, in some cases, fibrosis (e.g., CCl_4[9–11], DMN[12–14], TAA[15–17], DDC[18], APAP[19–22] and ethanol[23–25]) [26]. However, hepatotoxin-based approaches take months to develop liver injury and are therefore less amenable to rapid biological discovery. More recently, genetically encoded ablation models have been developed that enable specific liver cell types to be depleted (e.g., DTA[27] and NTR [28]). Each of these models have unique advantages and disadvantages; however, collectively they have led to remarkable advancements in our understanding of liver disease and regeneration.

Motivated to have a model of liver injury that is spatially localised yet retaining hallmarks of inflammation and fibrosis, we sought to adopt the cryoinjury approach successfully deployed in the cardiac field[3–5]. To this end, here we describe the development of a hepatic cryoinjury model of liver regeneration in this manuscript. We show that the hepatic cryoinjury model has no impact on survival and reproducibly leads to the liver regenerating within 30 days. Importantly, we observe that cryoinjury triggers an inflammatory phase associated with the clearance of necrotic and fibrotic tissue, followed by subsequent proliferation of hepatocytes at the injury site. A significant advantage of this model is that it enables the comparative analysis of healthy and injured parenchyma in a single animal. We anticipate that this hepatic cryoinjury model will facilitate the discovery of the cellular and molecular underpinnings of fibrosis and regeneration.

RESULTS

Hepatic cryoinjury in adult zebrafish induces localised cell death

We developed a novel method to study liver regeneration upon a localised cryoinjury of one of the liver lobes. Out of the three lobes present in the zebrafish liver, we chose the ventral lobe due to its surgical accessibility. In preparation for the surgery, zebrafish were immersed in

anaesthetic and placed ventrally facing up in a foam holder (Figure 1A). To create a reproducible and stereotypical injury, we performed all injuries at the level of the anterior fins and toward the midline. First, a small incision was performed to expose the liver (Figure 1B). Once the liver was visible, the excess water was gently removed using a rolled tissue. Then, the cryoinjury probe, which was cooled in liquid nitrogen for one minute, was placed on the liver surface for 15 seconds until thawing (Figure 1C). Fish were quickly transferred into a freshwater tank and reanimated by pipetting water into their gills for 30 seconds (Figure 1D).

To assess the extent of cauterisation following cryoinjury, we employed TUNEL staining in liver sections of adult zebrafish with hepatocytes labelled by Hnf4, comparing sham and 1 day post-cryoinjury (dpci, Figure 1E-F) livers. Sham-operated animals showed no TUNEL$^+$ staining (Figure 1E-E'). In contrast, cryoinjury caused an injured area (IA) comprised of TUNEL$^+$ cells surrounded by viable Hnf4$^+$ hepatocytes (Figure 1F-F'). To determine the extent to which this injury model induces apoptosis, we performed cryoinjury in *Tg*(*fabp10a:H2B-GreenLantern; actb2:annexinV-mKate*) adult zebrafish in which apoptotic cells will be labelled with the *mKate$^+$ signal* (Figure 1G-J). While we did not detect apoptosis in sham-operated animals (Figure 1G-H), *annexinV-mKate$^+$* apoptotic cells were observed around the injured area at 1 dpci, which can be easily detected by the localised loss of GreenLantern$^+$ hepatocytes (Figure 1I-J). Interestingly, the *annexinV-mKate$^+$* cells were distributed in an annular field around the injured area, but not in the central region (Figure 1J). Together, these results suggest that hepatic cryoinjury induces a localised cell death response characterized by a central necrotic core surrounded by a region of apoptotic cells at the injured border area.

Liver regenerates upon cryoinjury in adult zebrafish

To understand the temporal dynamics of liver regeneration upon cryoinjury, we examined the extent of recovery at different times post cryoinjury using *Tg*(*fabp10a: NLS-mCherry)* zebrafish livers. Dissected livers were cleared, rendering them transparent, and subsequently scanned using *in toto* confocal imaging of the gastrointestinal block (Figure 2A-G, Supplementary Figure 1A-E and Supplementary Figure 2A-I).

Hepatic cryoinjury induced severe damage in the ventral lobe at 1 dpci, which was evident by the loss of hepatocyte reporter fluorescence compared to a sham-control (Figure 2B-C, Supplementary Figure 2B-C, and Supplementary Figure 3A-C). However, we observed high survival rates throughout this surgical procedure (Supplementary Figure 2J; average= 91.33 %; n=302). We observed a gradual recovery of mCherry$^+$ hepatocyte expression from 3 dpci onwards, reducing the injured area's size (Figure 2D and Supplementary Figure 2D).

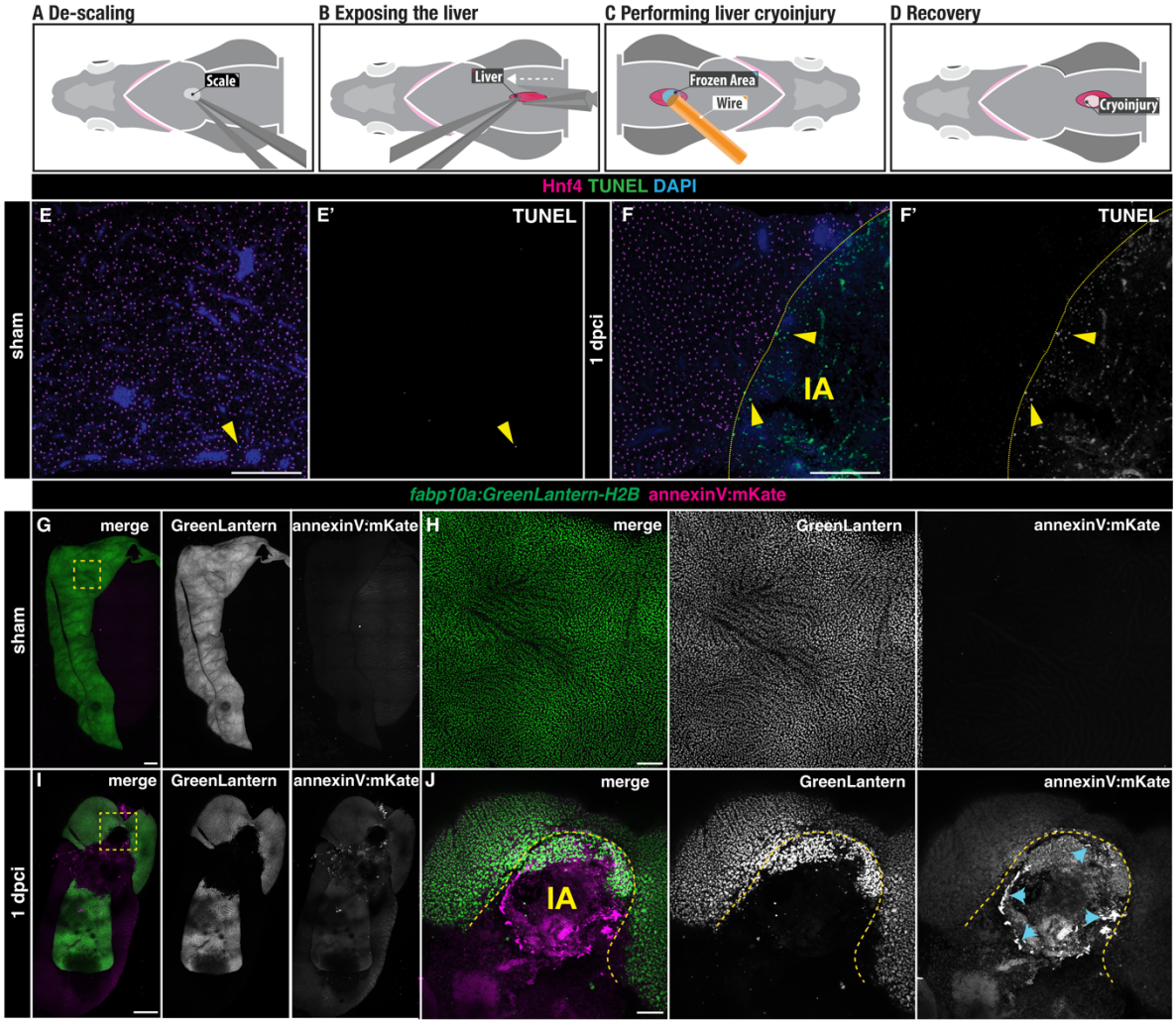

Figure 1. Liver cell death following cryoinjury. A-D) A simplified schematic illustrating the cryoinjury procedure in the zebrafish liver. A) The zebrafish liver is placed ventral side up to facilitate the surgery. B) A small incision near the midline exposes the ventral liver lobe. C) The frozen cryoprobe is applied to the liver surface for 15 seconds to induce injury. D) The damaged area in the liver appears as a blister-like structure at 1 dpci. E-F) TUNEL-staining of sham (E-E') and injured (F-F') liver sections at 1 dpci. IA, injured area. Yellow arrowheads: TUNEL$^+$ cells; yellow dashed lines: border zone. G-J) *Tg(fabp10a: GreenLantern-H2B; annexinV:mKate) in toto* acquisitions of sham (G-H) and 1 dpci (I-J) livers. I-J) The IA (yellow dashed line) is identifiable by the absence of *GreenLantern-H2B*$^+$ hepatocytes. Blue arrowheads: *annexinV-mKate*$^+$ cells. Scale bars: 500 μm.

At 7 dpci, when other liver injury models have fully regenerated[7,8,20,29], the site of insult is still clearly visible in cryoinjured livers (Figure 2E and Supplementary Figure 2E). The injured area is almost fully repaired at 14 dpci, as regeneration progressed (Figure 2F and Supplementary Figure 2F). Prolonged follow-up at 3, 5, 8 months post-cryoinjury (mpci) and 1 year post-cryoinjury (ypci) showed a fully regenerated liver parenchyma (Figure 2G, Supplementary Figure 2H-I, and Supplementary figure 3D). Quantifying the injured area as a percentage of the total liver area at the different time points collected through this study indicates that the liver regenerates progressively over two weeks (Figure 2H). Collectively, these results establish the hepatic cryoinjury model as a reproducible approach to induce a spatially localised injury that is repaired over several weeks.

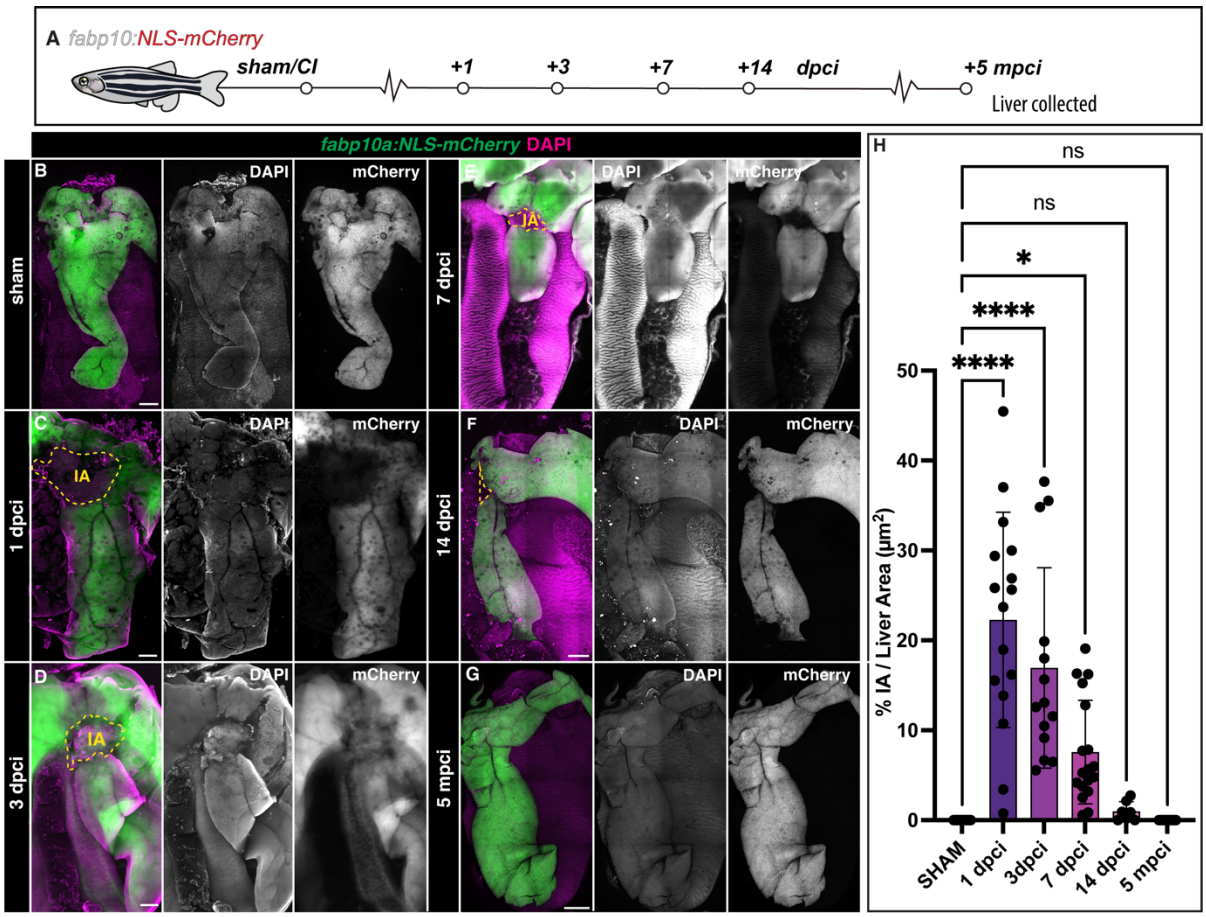

Figure 2. Progression of liver regeneration following cryoinjury. A) A simplified schematic illustrating the collection of livers following cryoinjury. B-G) Whole mount images of cleared zebrafish livers at the indicated stages of regeneration. Yellow dashed lines: border zone. H) Quantification of the IA area compared to the visible liver parenchyma area (n= 16, 16, 14, 18, 7, and 12 bars indicate mean, *p*-values: one-way ANOVA followed by Tukey's multiple comparisons test). Scale bars: 500 μm.

Hepatic cryoinjury induces a transient fibrotic response

Fibrosis is an evolutionarily conserved mechanism of liver repair that is beneficial when transient but can be maladaptive in chronic liver disease[2]. Given the extent of cell death observed following cryoinjury, we wanted to determine whether this injury model involved a fibrotic response. To this end, we used the Fuchsin Orange G (AFOG) staining[5,30] to determine changes in ECM in response to cryoinjury. In the sham zebrafish liver, we mostly detected collagen surrounding the basement membrane of major blood vessels (Figure 3A). At 1 dpci, the insulted liver tissue started to develop collagen and fibrin deposition at the IA (Figure 3B), which gradually increased (Figure 3C-E), reaching a fibrotic peak at 5 dpci (Figure 3D, Figure 3H, and Supplementary Figure 4A-B). Immunofluorescence staining with a collagen type I specific antibody revealed the presence of interstitial collagen depositions in the IA at 5 dpci (Figure 3H-H'''), which is absent in sham-operated animals (Figure 3G-G'''). Segmentation and quantification of the collagen staining confirmed a significant increase in collagen deposition at 5 dpci compared to sham-operated livers (Figure 3G-I). During the following two weeks, fibrosis was

gradually cleared and was almost undetectable at 30 dpci (Figure 3F), when the liver parenchyma structure was fully restored. These results suggest that hepatic cryoinjury in the zebrafish leads to the formation of a transient fibrotic deposition, which is resolved within 30 days.

Hepatic cryoinjury triggers a transient inflammatory response

The initial phase of liver regeneration is often associated with inflammation as leukocytes infiltrate the injured liver tissue[2,31]. Leukocytes are responsible for the phagocytosis of apoptotic and necrotic cells and the secretion of cytokines that promote hepatocyte survival and proliferation during liver tissue repair. To assess whether hepatic cryoinjury caused inflammation, we stained liver sham-operated and injured sections of *Tg*(*fabp10a*:NLS-mKate) zebrafish, carrying hepatocyte-specific mKate$^+$ nuclear transgene expression in combination with the pan-leukocyte marker L-plastin (Lcp1) antibody. In homeostatic livers, we observed a few Lcp1$^+$ leukocytes in the liver tissue (Figure 4A). However, we detected a rapid infiltration of inflammatory cells after injury, at 1and 3 dpci, both in the healthy parenchyma and the cryoinjured area (Figure 4B and 4F). Immune infiltration was maintained for 7 days post-injury in the healthy liver parenchyma and the insulted area (Figure 4C-D).

The presence of leukocytes gradually decreased at 18 dpci (Figure 4E), and to basal levels at 30 dpci (Figure 4F), when the damaged area could not be detected. Analysis and quantification of sections of sham-operated and injured liver sections at different timepoints with Lcp1$^+$ staining showed significantly increased of infiltrating leucocytes at operated livers at 1, 3, 5, and 7 dpci (Figure 4F). These experiments confirm that hepatic cryoinjury is associated with the local and transient infiltration of leukocytes into the injured area.

Cryoinjury induces both localised and distal compensatory hyperplasia

Two regenerative mechanisms could be at play in the cryoinjury model, namely compensatory hyperplasia, in which hepatocyte proliferation occurs throughout the parenchyma until liver mass reaches homeostasis, or epimorphic regeneration, in which hepatocytes proliferate in a spatially localised region around the injury. In order to understand the regenerative response upon hepatic cryoinjury, we examined hepatocyte proliferation. To identify proliferative hepatocytes we stained sections of *Tg(fabp10a:NLS-mKate)* with the proliferating cell nuclear antigen (PCNA) antibody, and performed BrdU pulse-labelling studies, injecting BrdU in sham and injured zebrafish at 2 dpci. Quantification of hepatocyte proliferation (mKate$^+$/PCNA$^+$) confirmed that there were few mKate$^+$/PCNA$^+$ cells and mCherry$^+$/BrdU$^+$ HCs in sham-operated animals (Figure 5A and Supplementary Figure 5A-G), consistent with the slow turnover of hepatocytes in adulthood during homeostasis[32–34]. In contrast, proliferating hepatocytes were significantly more abundant around the injured area during the first week of recovery after cryoinjury (Figure 5B-D and Supplementary Figure 5H-S).

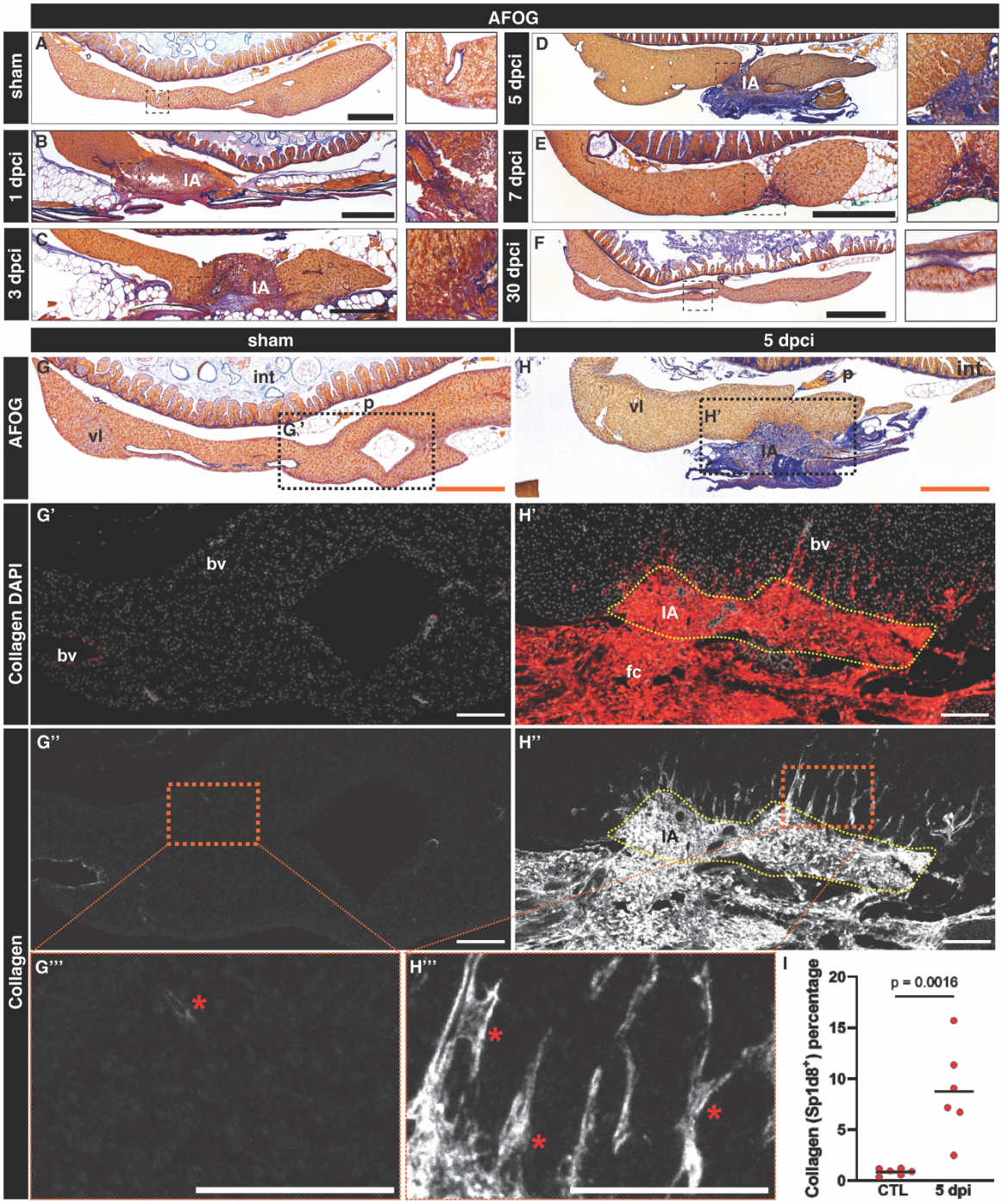

Figure 3. Transient fibrotic deposition during liver regeneration following cryoinjury. A-H) AFOG staining in sections of representative sham-operated (A,G) or injured livers at the indicated stages (B-H). Blue: collagen; Red: cell debris and fibrin. Anterior is towards the left, dorsal is towards the top. Details are shown at higher magnifications. G'H') Adjacent sections from the samples showed in G and H, immunostained with an anti-Col1a1 antibody and counterstained with DAPI. Asterisks: Col1a1 deposition in the liver parenchyma. I) Quantification of the collagen area of livers from the indicated cohorts, normalized to the liver parenchyma area (n=6; solid black line indicated the mean; *p*-value: unpaired Student's *t*-test). Bv: blood vessel; fc, fibrotic cap; IA: injured area; int: intestine; p: pancreas; vl: ventral lobe. Scale bars: 100 (white), 500 μm (orange and black).

Hepatocyte proliferation peaked between 3 and 7 dpci, which correlates with the timing of reduction in the IA (Figure 5F and Supplementary Figure 5L-M). Analysis of proliferating hepatocytes (mKate^{+}/PCNA^{+} or

mCherry+/BrdU+) shows a localised hyperplasia, with higher density of mKate+/PCNA+ or mCherry+/BrdU+ hepatocytes in areas surrounding the injured area (Supplementary Figure 5L-M and R-S). This recovery of hepatocytes around the cryoinjured area is consistent with an epimorphic regeneration. However, when we extend our analysis of the location of mKate+/PCNA+ or mCherry+/BrdU+ HCs, we observe the presence of proliferating hepatocytes throughout the liver parenchyma (Supplementary Figure 5H-M and 5T-Y), including the contralateral lobes (Supplementary Figure 5T-Y), which is indicative of compensatory hyperplasia. Hepatocyte proliferation decreased during later stages of regeneration to a baseline at 30 dpci (Figure 5E-F). In light of these studies, we determined that hepatic cryoinjury stimulates features of both epimorphic and compensatory hyperplasia during liver regeneration.

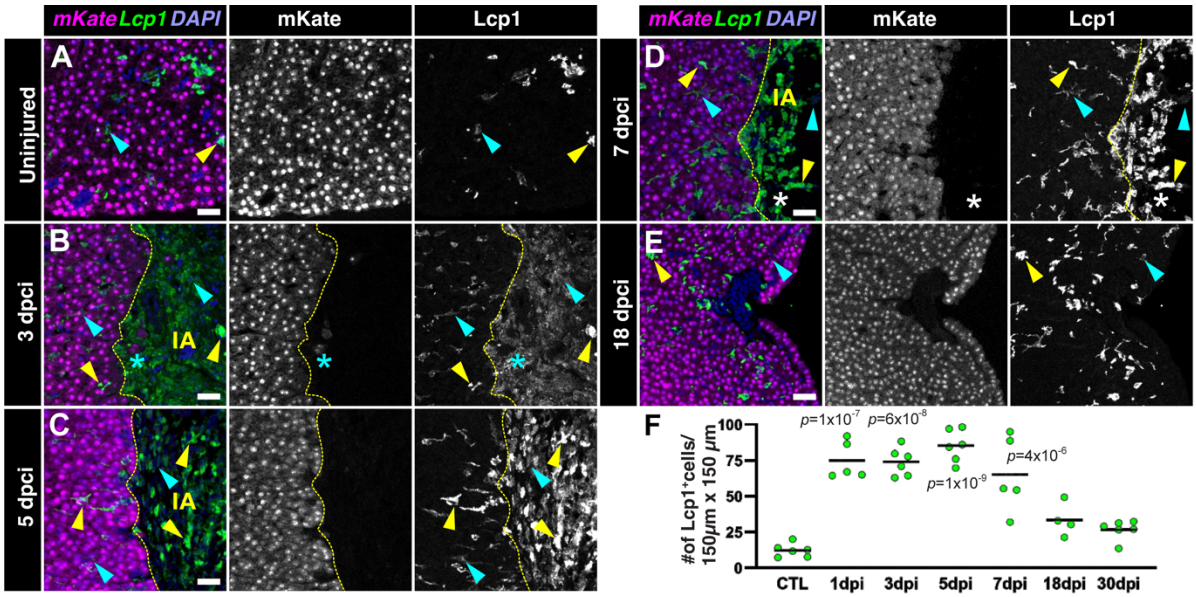

Figure 4. Cryoinjury induces the local and transient infiltration of leukocytes. A-E) Sections of livers from *Tg(fabp10a:NLS-mKate)* animals at the indicated stages, immunostained to detect hepatocyte nuclei (mKate) and leukocytes (Lcp1) Cyan arrowheads: low signal Lcp1+cells; dashed yellow line: border zone; IA: injured area; yellow arrowheads: high signal Lcp1+ cells; Asterisks: spared hepatocytes surrounded by injured/necrotic tissue area. (H) Quantification of the number of Lcp1+ cells in designated regions (n = 6, 5, 6, 6, 5, 4, and 6; solid black line indicates the mean). *p*-values: one-way ANOVA followed by Tukey's multiple comparisons test. Scale bars: 25 μm.

The biliary and endothelial network is re-established during regeneration

Adaptive liver regeneration that recovers hepatic function requires appropriate restoration of the biliary and vascular network, which are comprised of biliary epithelial cells (BECs) and liver sinusoidal endothelial cells (LSECs), respectively.

To examine whether BECs were regenerating following hepatic cryoinjury, we collected *Tg(fabp10a:GreenLantern-H2B)* livers at 1, 3, 7, and 21 dpci (Figure 6 A-E and Supplementary Figure 6 A-C), performed CUBIC clearing and immunostaining against the BEC marker Annexin A4 (Anxa4), and imaged livers via confocal imaging. Anxa4+ BECs were detectable throughout the liver parenchyma in sham livers (Figure 6A-A'').

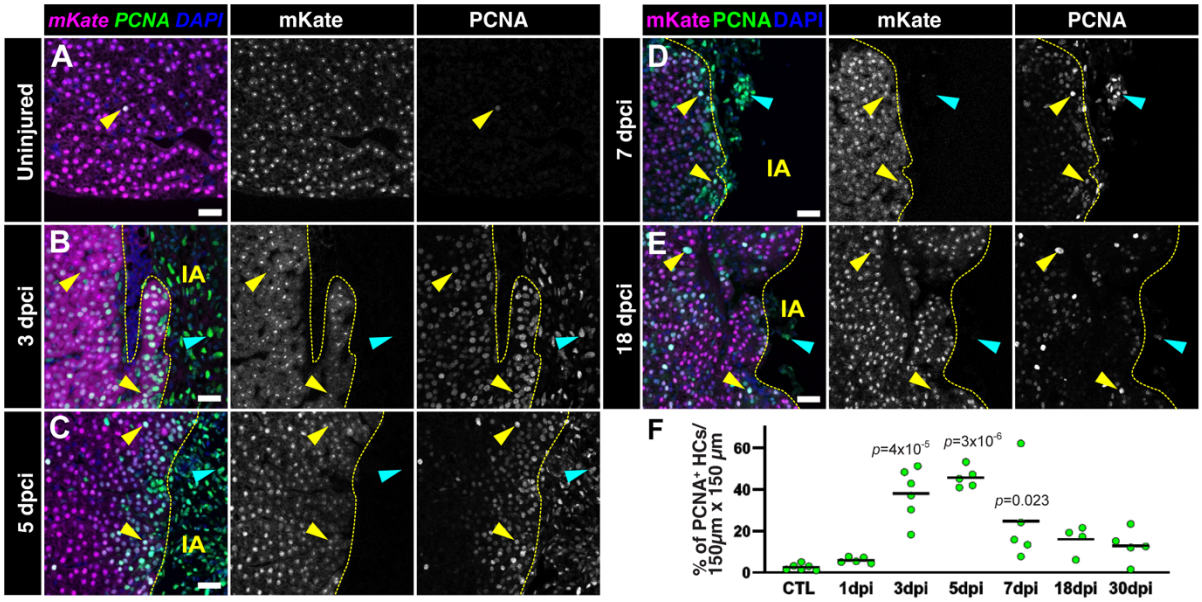

Figure 5. Local hepatocyte hyperplasia upon cryoinjury. A-G) Liver sections from *Tg(fabp10a:NLS-mKate)* animals at the indicated stages, immunostained to detect proliferation (PCNA) and hepatocyte nuclei (mKate). Yellow arrowheads: proliferating hepatocytes. Cyan arrowheads: other cell types actively cycling. Dashed yellow line: separation between healthy and injured liver parenchyma; IA, injured area; Asterisks: spared hepatocytes surrounded by injured/necrotic tissue area. H) Hepatocyte proliferation index in the border zone at the indicated stages (n = 6, 5, 6, 5, 5, 4, and 5; solid black line indicates the mean). *p*-values: one-way ANOVA followed by Tukey's multiple comparisons test. Scale bars: 25 μm.

However, the distribution of Anxa4+ BECs was disrupted in the IA at 1 and 3 dpci, indicating that bile duct structures were affected during this procedure (Figure 6B-C and Supplementary Figure 6B-C). A progressive recovery of the biliary network was observed at 7 and 21 dpci, as the insult area gradually reduced in size (Figure 6D-E and Supplementary Figure 6B-C). Importantly, no differences were observed in the architecture of the biliary network in regenerated liver tissue at 21 dpci compared to sham-operated liver tissue, and consistent with the regenerative response in hepatocytes (Figure 6A'', Figure 6E'', and Supplementary Figure 6 B-E).

To study if liver sinusoidal endothelial cells (LSECs) were regenerating upon cryoinjury in the adult liver, we collected *Tg(fli1a:NLS-eGFP)* livers at 1, 3, 7, and 30 dpci (Figure 6F-J and Supplementary Figure 6 F-G). Livers were acquired by *in toto* confocal imaging. eGFP+ LSECs were observed equally through the sham liver parenchyma (Figure 6F-F'' and Supplementary Figure 6F-G). However, the vasculature LSECs distribution was affected in the IA at 1 dpci (Figure 6G-G'' and Supplementary Figure 6F-G). Vascular recovery starts to be observed at 3 dpci, with branching morphogenesis of eGFP+ LSECs appearing within the IA (Figure 6H-H'' and Supplementary Figure 6F-G) at early stages that previously described in liver regeneration literature[35]. Interestingly, eGFP+ LSECs are detected throughout the entire IA at 7dpci, revealing that vasculature regeneration precedes HCs

and BECs regeneration (Figure 6I-I'' and Supplementary Figure 6F-G). eGFP+ LSECs at the IA (Figure 6I'') seemed thicker and organised differently to ECs in the sham liver parenchyma (Figure 6F''). At 30 dpci, when the liver is fully regenerated, eGFP+ LSECs appeared to have a most disorganised pattern at the IA (Figure 6J-J'') compared to sham (Figure 6F-F'').

These findings demonstrate that hepatic cryoinjury disrupts the biliary and vasculature network, which is subsequently re-established during liver regeneration.

Characterization of the transcriptional landscape following cryoinjury

To study the transcriptional changes that occur during liver regeneration, we performed bulk RNA-seq on the injured region of livers dissected from *Tg(fabp10a:NLS-mCherry)* animals following sham-operation, 1, 3, and 7 dpci (Figure 7A and Supplementary Figure 7A-C). At 1 dpci, we detected 438 upregulated genes and 981 downregulated genes when compared to sham-control liver (Figure 7B and 7E-F). Gene Set Enrichment analysis (GSEA) identified the unfolded protein response pathway (p-value: 0.074; Normalised enrichment score (NES): -1.40), a well-established component of the integrated stress response, as amongst the most enriched signatures following cryoinjury (Figure 7G and Supplementary Figure 7C). We also identified enrichment for signatures associated with TNFα signalling (p-value: 0.318; NES: -1.19) and TGF-β signalling (p-value: 0.235; NES: -1.16), consistent with the inflammatory and fibrotic features exhibited following cryoinjury (Figure 7G). Many of the downregulated hallmarks and Gene Ontology (GO) enrichment (Figure 7G and Supplementary Figure 7B), which we observed following cryoinjury at 1dpci, are associated with housekeeping functions of hepatocytes, such as bile acid metabolism (p-value: 0.02; NES:1.87), xenobiotic metabolism (p-value: 0.037; NES:1.75), and fatty acid metabolism (p-value: 0.05; NES:1.65) (Figure 7G). At 3 dpci, 167 upregulated differentially expressed genes (DEGs) were detected, while 163 DEGs were downregulated (Figure 7C and E-F) compared to the sham. GSEA of DEGs at 3 dpci revealed several hallmarks related to cell proliferation and migration, including the G2/M checkpoint signature (p-value: 0.000; NES: -1.55) and epithelial-mesenchymal transition signature (EMT; p-value: 0.000; NES: -1.76) respectively (Figure 7G). These signatures are consistent with the timing of proliferation described following cryoinjury (Figure 5B), and the increased inflammation and recruitment of leukocytes to the injured area in livers between 3 dpci and 7 dpci (Figure 4B and D). To infer changes in tissue composition following cryoinjury, we used cell-type specific genes to identify the dynamics of liver regeneration on the different cell types present in the liver during the first 7 dpci (Figure 7H). At 1 dpci, we observed a subtle increase in genes specifically expressed in endothelial cells and hepatoblast (Figure 7H), which may be indicative of angiogenesis and dedifferentiation of hepatocytes to a hepatoblast-like state.

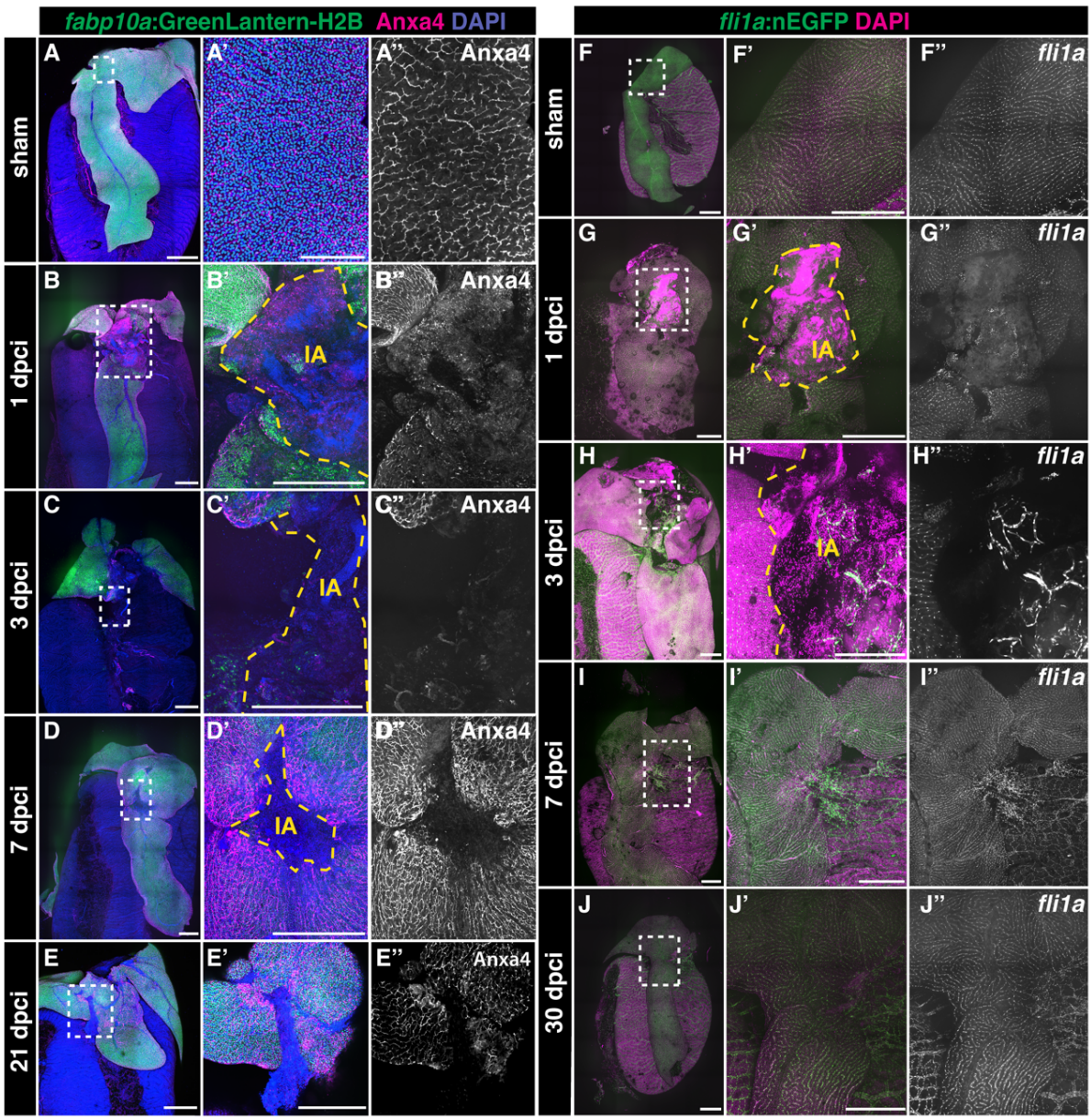

Figure 6. Biliary Epithelial Cells (BECs) and endothelial cells (LSECs) recover upon cryoinjury. A-E) Whole mount imaging of *GreenLantern*+ hepatocytes and Anxa4+ biliary epithelial cells from sham (A) or injured (B-E) livers at the indicated stages. Details from boxed regions are shown magnified. F-J) Whole mount acquisitions of GFP+ LSECs from sham (F) or injured (G-J) livers at the indicated stages. Details from boxed regions are shown magnified acquisitions. Dashed line: border zone of the injured area, IA: injured area. Scale bars: 500 μm.

Genes associated with immune cells were enriched at 1 dpci upon injury, consistent with the early recruitment of immune cells towards the site of injury (Figure 7H). At 3 dpci, we detected enrichment in genes specifically expressed by BECs, suggesting an active restoration of the biliary network (Figure 7H). By 7 dpci, we detected 97 upregulated and 290 downregulated DEG compared to sham-operated livers (Figure 7D and E-F). This observation might indicate a gradual shift towards homeostasis in the liver. In light of these studies, we conclude that the transcriptional landscape dynamically changes during regeneration as the liver responds to cryoinjury, undergoes regenerative growth and eventually returns to homeostasis.

Discussion

Here, we introduce the hepatic cryoinjury model, which serves as a rapid and reliable method to investigate liver regeneration in a spatially localised manner (Figure 8 and Table 1). The frozen cryoprobe's contact with the liver surface generates a necrotic region, surrounded by apoptosis in the injured border area, resembling clinical liver injuries[36]. Furthermore, necrotic cells trigger a robust innate immunological response and immune infiltration at the injury site. The hepatic cryoinjury model offers several advantages compared to the other injury models (Table 1). Firstly, it creates a distinct localized injury, enabling the examination of injured and uninjured hepatic parenchyma in the same animal. Moreover, hepatic cryoinjury is easy to perform and visualise macroscopically (blister formation), which facilitates the investigation of the tissue regenerative microenvironment and the utilization of state-of-the-art sequencing and imaging techniques. Secondly, the cryoinjury model gives rise to necrotic and apoptotic tissue, and the localised infiltration of inflammatory cells, which are absent in other surgical models (i.e., HPx). Thirdly, the hepatic cryoinjury model induces a transient fibrotic response not seen in other models, which resolves within 30 dpci without hindering liver repair. For these reasons, we anticipate that this unique model will aid in the discovery of the molecular mechanisms of fibrosis and regeneration.

Although the HPx model is almost 90 years old, it remains the gold standard of models to study liver regeneration. Liver regeneration in rodent HPx models occurs rapidly via compensatory hyperplasia, in which hepatocyte proliferation peaks at 24 hr post resection, before receding by 3 days and liver homeostasis is re-established at 7 days [7,8]. Zebrafish HPx models show similar dynamics of hepatocyte proliferation with almost no detectable proliferative beyond 4 days[7,8]. A major point of difference between the HPx models and hepatic cryoinjury is the more prolonged time course of regeneration (30 days). We suspect this is partly due to transient fibrosis and the need to resolve damaged tissue before mounting a proliferative phase of regeneration.

Acetaminophen (APAP) overdose is the most common cause of acute liver failure (ALF), as it induces necrosis of pericentral hepatocytes, leading to a necrotic area in zone 3 of the liver parenchyma[21]. The APAP model shares features of the hepatic cryoinjury model, such as the induction of region-specific necrosis (Table 1). However, one major distinction is that due to its mechanism of action, APAP targets pericentral hepatocytes, whereas the hepatic cryoinjury affects all cells present at the site of injury. Tissue loss due to APAP exposure is recovered by hepatocyte proliferation within 4 days, peaking at 2 days post APAP exposure[29], which is similar to the kinetics of hepatocyte proliferation observed following HPx but earlier than we have observed following hepatic cryoinjury. Interestingly, hepatocyte proliferation following APAP exposure occurs in areas where healthy hepatocytes are in contact with necrotic tissue, rather than via compensatory hyperplasia[37], which is reminiscent of the epimorphic proliferative response observed following cryoinjury. Another similarity between cryoinjury and APAP, is that APAP exposure triggers the infiltration of immune cells, activating an innate and adaptive immunological response[21]. Given the crucial role of immunity in liver disease, it is beneficial

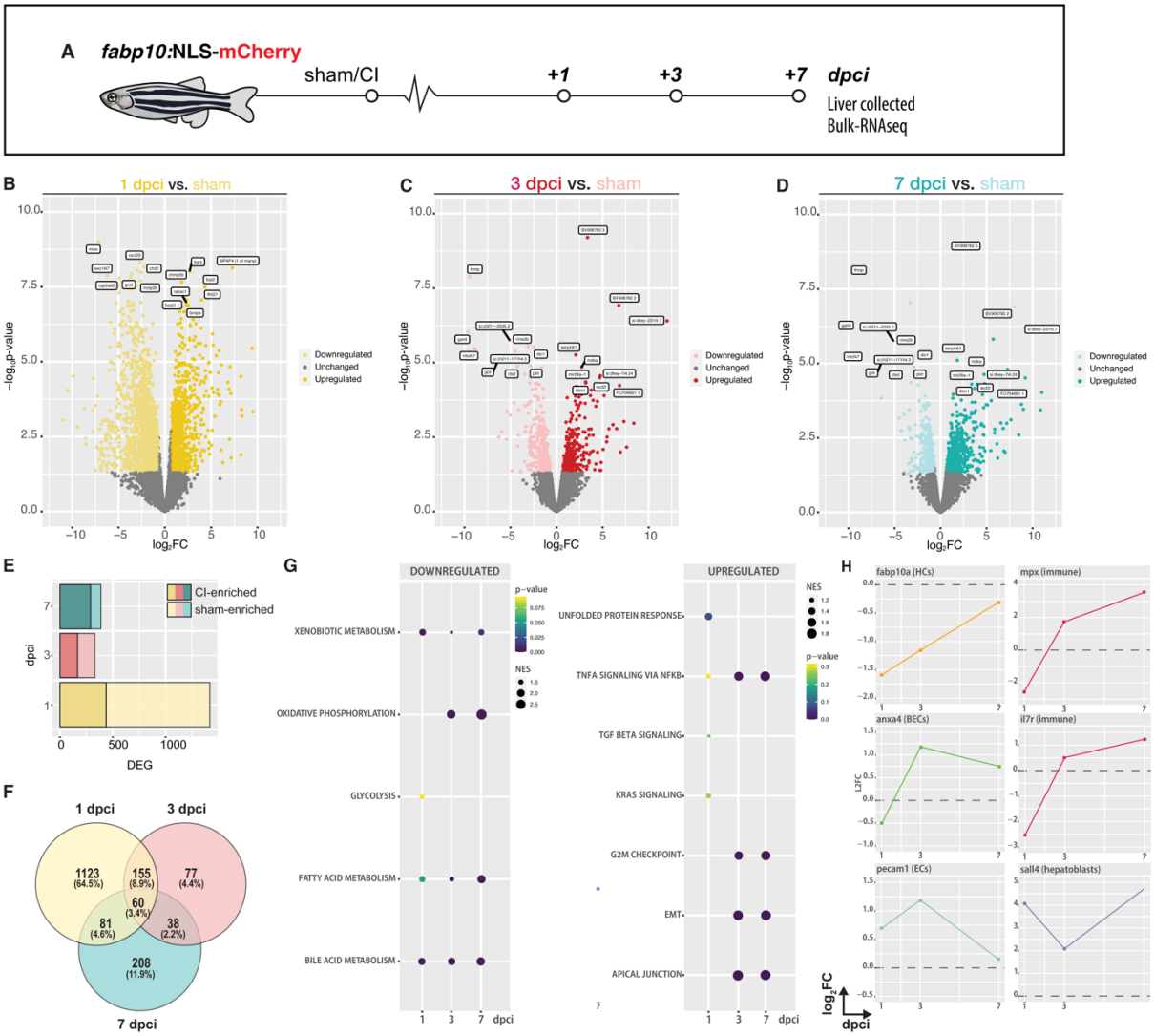

Figure 7. Transcriptional signatures of liver regeneration upon cryoinjury. A) Schematic representation of the experiment workflow. B-D) DEGs (FC ≥1.5 (darker dots) or ≤-1.5; *P*≤0.05; lighter dots) with top DEG annotated. E) Bar plot representing the number of upregulated and downregulated DEG at 1, 3, and 7 dpci. F) Venn diagram representing DEG at 1,3, and 7 dpci. G) GSEA-enrichment of liver cell types during liver regeneration. H) Gene expression dynamics of key genes for specific liver populations.

that the hepatic cryoinjury model exhibits classic hallmarks of inflammation.

Genetic ablation models provide an invaluable approach for targeted cell ablation in animal models, elucidating the roles of various cell populations in liver tissue repair and regeneration[38,39] (Table 1). These models have significantly contributed to our understanding of transdifferentiation events between BECs and hepatocytes in the context of tissue regeneration. While the ability to selectively target specific cell populations presents clear advantages, generating cell type-specific promoter transgenic lines can be labour-intensive and time-consuming. In contrast to the cryoinjury model, which affects all parenchymal and non-parenchymal cells in the liver, cell-specific ablation techniques uniquely target distinct liver cell populations, thereby only allowing for the investigation of the function of a unique liver cell of interest.

Liver fibrosis is a critical feature in the development of chronic liver diseases and the progression towards hepatocellular carcinoma (HCC). Hepatic cryoinjury leads to a transient fibrotic response (peaking at 5 dpci) that was resolved within 30 dpci. Compared to other models of liver fibrosis (e.g., CCl_4, TTA, ethanol or DDC), which typically develop over months[26] (Table 1), fibrosis in the cryoinjury model occurs rapidly and is resolved over time. In future studies, the cryoinjury model could be used to explore the clonality of fibrosis and regeneration. To this end, recent advances in DNA-barcoding lineage tracing methods[40–44] and spatial transcriptomics[45,46] make it feasible to use the cryoinjury model to identify the mechanisms driving the resolution of fibrosis. This enhanced understanding is crucial for identifying innovative therapeutic strategies promoting liver repair and combating fibrotic progression.

In summary, we have described a new hepatic cryoinjury and regeneration model that recapitulates key features of liver disease (Figure 8). Given the rapid and reproducible nature of the technique, we suspect the model will offer opportunities to uncover the molecular underpinnings of liver regeneration.

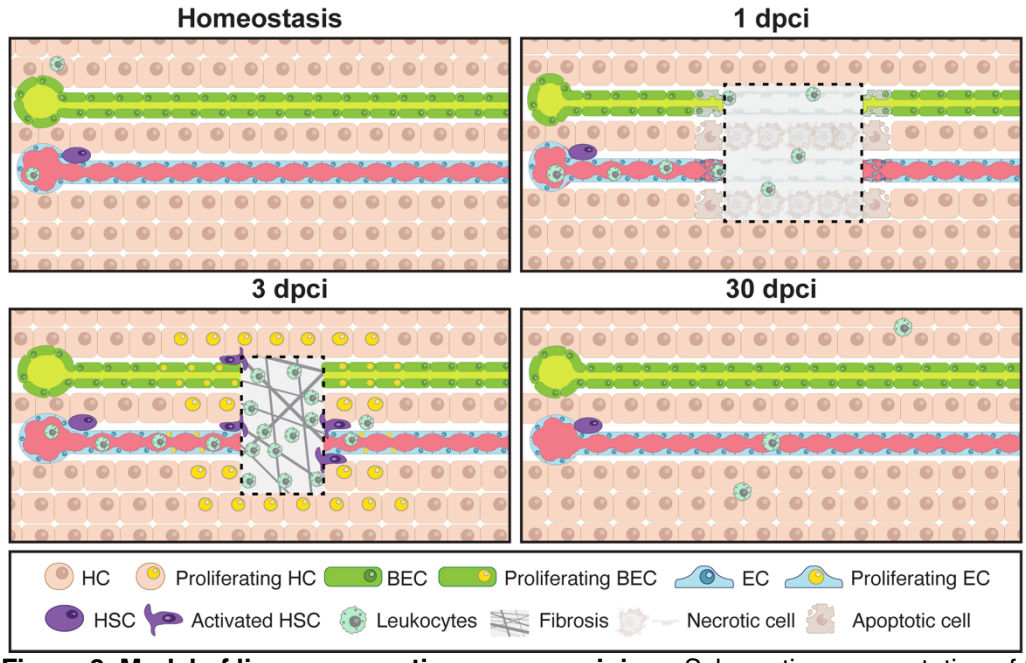

Figure 8. Model of liver regeneration upon cryoinjury. Schematic representation of the cellular events upon cryoinjury during liver repair in the zebrafish

Material and methods

Experimental model and details

Experiments were conducted with adult zebrafish (Danio rerio) aged 4-9 months raised at a maximal 5 fish/L and maintained under the same environmental conditions: 27.5-28C, 650-700ms/cm, pH 7.5. The lighting conditions were 14:10 hours (Light: Darkness) and 10% of water exchange a day. Experiments were approved by the Peter MacCallum Cancer Centre AEEC (E665). All animal procedures conformed in accordance with the Prevention of Cruelty to Animals Act, 1986 (the Act), associated Regulations (2019) and the Australian code for the care and use of animals

for scientific purposes, 8th edition, 2013 (the Code). The following transgenic zebrafish lines were used in this study: *Tg(fabp10a:NLS-mCherry), Tg(fabp10a:GreenLantern-H2B), Tg(fabp10a:NLS-mKate), Tg(fli1a:nEGFP).*

Cryoinjury and analysis of the injured area

Fish are immersed in Tricaine (0.032%; wt/vol; Sigma) before surgery and placed in a foam holder with the ventral area facing up. Under a stereo microscope, scales above the liver area are removed using sharp forceps. Once the area had been cleaned, a small incision parallel to the skin using micro-dissecting scissors towards the midline and the anterior fin was made to expose the liver through the ventral zebrafish body. Once the liver is exposed, the excess water is removed using tissue paper (KimWipe). The cryoinjury probe of 1mm diameter (Jaycar; Australia), which is cooled in liquid nitrogen for one minute, is placed on the liver surface for 15 seconds until thawing. Sham operations consisted of placing the thawed cryoprobe on the exposed liver at room temperature. Fish are quickly placed in a freshwater tank and reanimated by pipetting water into their gills for 30 seconds. The complete surgical procedure takes 3-5 minutes per fish. Healthy fish should be swimming normally after 5 minutes. Fish are transferred to the normal tanks into their racks 10 minutes after surgery with a gentle water flow. The damaged tissue was easily identified either from the lack of fluorescence when using HCs specific promoter line, which expresses a nuclear mCherry or GreenLantern signal specifically in HCs, or a blister-like injury in the liver surface. Injured and SHAM livers were phenotyped, and acquisitions were performed using a Leica M165FC fluorescent stereomicroscope. The injured area was measured on Imaris Software 9.0 (Bitplane). Statistical analysis and graphs were generated using GraphPad Prism v9.

Whole-Mount CUBIC Liver Immunofluorescence and image processing

In toto immunofluorescence was performed as described[47] .Animals were euthanized at different times post-injury by immersion in 0.16% Tricaine. Livers were collected and fixed in PFA 4% overnight at 4 degrees in rocking agitation. We washed the livers 3 times in PBS Tw 0.1% before transferring them to CUBIC-L[48] for 18h at 37C. After CUBIC-L incubation, livers were washed in PBS1x three times for 15 minutes. Livers were incubated with blocking solution (5% BSA, 5% got serum, 0.1% Tween-20) overnight. Primary and secondary antibodies were incubated for one day at 4C in rocking agitation. Livers were transferred to CUBIC-R$^+$ for 2 hours at room temperature and embedded in CUBIC-R$^+$-Agarose for imaging. Livers were mounted on a glass bottom culture dish (MatTek Corporation) for confocal acquisition. Whole liver acquisitions were obtained with Zeiss LSM 780 and Nikon Sora Spinning-Disk confocal microscopes using 10X dry and 20X dry lenses. Images were acquired at 512x512 or 1024x1024 resolution. For every liver acquisition, tile-scan and z-stack modules were used to acquire a representative area of the liver. The injured area of the liver in whole-mount acquisitions was analysed and measured on Imaris Software 9.0 (Bitplane) and Fiji[49]. Acquisitions were saved as TIFF or JPEG on Fiji of the original files.

BrdU$^+$ and PCNA$^+$ hepatocytes image analysis

Adult zebrafish were injected intraperitoneally at 2 dpi with 20 µl of 2.5 mg/ml of 5-Bromo-2-deoxyuridine (BrdU, B5002-1G, Sigma). Livers were collected and

processed for analysis at 5 dpci. *in toto* immunofluorescence was performed as described[47] .Whole-mount IF was performed using anti-BrdU (Abcam # ab6326 [BU1/75 (ICR1), rat), anti-RFP (Abcam #ab62341, rabbit), Goat anti-Rat IgG (H+L) Cross-Adsorbed Alexa Fluor 647 (ThermoScientific), and Goat anti Rabbit IgG (H+L) Alexa Fluor 594 Antibody (Invitrogen). Using Imaris Software 9.0 (Bitplane), we used the co-localisation channel tool to create a new channel, which represents BrdU$^+$ HCs. A spot segmentation of BrdU$^+$ HCs and BrdU$^-$HCs was created. Manually, the site of injury was created as a surface. We used the new injured area surface and the ImarisXT/Distance-Transformation package (outside surface) to define the distance of every BrdU$^+$ HCs spot to the injury site. This new channel was masked into the BrdU$^+$ HCs spots, previously created. The novel BrdU$^+$ HCs spots channel contains the specific distance to the injured area from every proliferating HCs, named as Proliferating HCs distance channel. A new spot segmentation was done using the Proliferating HCs distance channel. We exported the Position X, Y, Z and Proliferating HCs distance channel mean intensity from the last Proliferating HCs distance channel. Spot segmentation. Using R, the different datasets were selected to create a representative graph, using ggplot2 package, of the presence of BrdU$^+$ HCs or PCNA$^+$ HCs towards the site of injury and quantified their location throughout the parenchyma with the injured area as the point of reference, and the density towards the slide or whole-mount acquisitions. These R scripts are available on GitHub (https://github.com/marcsmelon).

Zebrafish Liver Fixation and Histological Processing

To obtain histology sections for AFOG or immunofluorescence, adult zebrafish livers were collected with the rest of the gastrointestinal tract (GIT). This procedure minimized disruption of the fragile liver tissue. Adult zebrafish were euthanized by immersion in 0.16% tricaine and placed in ice-cold PBS. A ventral incision through the skin, muscle, and peritoneal cavity was made, starting at the anus towards the pericardiac cavity. To avoid disrupting adhesions and scar tissue at the injury zone in early injury time points (1-7 dpci), the tissue adhering to the liver injury was left intact on the liver by performing an incision surrounding it. The GIT was detached at its anal part and slowly lifted while cutting the vasculature connecting the dorsal part of the GIT to the peritoneum and gonads. Once completely lifted from the cavity, a final cut was made anteriorly on the esophagus to extract the GI. Samples were fixed overnight at 4°C in 10% Neutral Buffered Formalin (HT501125, Sigma) and embedded in paraffin following standard processing (45 min. incubations in ethanol 70%, 90%, 95%, 2 x 100%, 2 x xylenes, and 4x paraffin washes). 7 μm sagittal sections were mounted on SuperFrost+ slides (#12-550-15, Fisherbrand) and dried overnight at 37°C before storage or processing.

Acid Fuchsin-Orange G (AFOG) staining and imaging

For AFOG staining, sections were dewaxed and rehydrated using standard procedures and then stained as described[50]. Collagen was stained blue, while fibrin and cell debris appeared red. Sections were imaged on a Leica DM6-B upright microscope equipped with a Leica DFC7000 camera using the 10x or 20x objectives. Whole GIT images were acquired using the LAS-X software's automated navigator and stitching function.

Immunofluorescence in Paraffin Sections

Immunofluorescence was performed as described[3] with the following modifications. After dewaxing and rehydration, sections were heated and then pressure cooked for 4 min. in citrate unmasking solution (H3300, Vector, 100x dilution). Once cooled, sections were permeabilized for 10 min in methanol, washed in PBST (0.1% Tween 20 in PBS), and photobleached for 45 min to remove autofluorescence (PMID: 29993362). Slides were washed three times for 5 min in PBST before incubation in 0.25% Triton X-100 in PBS. After washing the slides in PBST and drawing hydrophobic rings (ImmEdge pen, H-4000, Vector) unspecific binding sites were blocked using 5% goat serum, 5% bovine serum albumin in PBST for 1 h at room temperature. Primary antibodies were incubated in blocking buffer overnight at 4°C in a humidity box. Primary antibodies used were, mouse anti-RFP (clone RF5R, MA5-15257 ThermoFisher; 1:1000), mouse anti-PCNA (SC-56, Santa Cruz Biotechnology; 1:500), Rabbit anti-Lcp1 (GTX124420, GeneTex; 1:500), mouse anti-col1a1 (clone Sp1.d8, DSHB; 1:20). Slides were washed three times for 5 min in PBST before incubation with secondary antibodies and DAPI as nuclear counterstaining in blocking buffer for 1 h at room temperature. Alexa conjugated secondary antibodies (Life Technologies, 1:500) were used to detect isotype-specific primary antibodies, except for the detection of Col1a1, which required a tyramide amplification step (Alexa Fluor 555 Tyramide SuperBoost Kit, Invitrogen). After staining, sections were quickly rinsed in double distilled water and mounted with Fluorsave reagent (345789, Millipore).

Histological Imaging and Analysis

After immunofluorescence, sections were imaged on a Zeiss LSM900 confocal microscope using the 10x or 20x objectives with 3-4 images per z-stack. Samples were imaged using the ZEN-pro software, and images were saved as multi-stack CZI files. Images were stacked in ImageJ, and individual channels were exported to TIF files. Multi-color images and color levels were adjusted using Adobe Photoshop, and figure panels were cropped and rotated to dimension in CorelDRAW.

To quantify hepatocyte proliferation, sections from *fabp10a:n-m*Kate livers were immunostained with anti-RFP and anti-PCNA antibodies (see above). Three sections containing the largest injury areas were imaged. n-mKate$^+$ and PCNA$^+$n-mKate$^+$ cells were counted manually using ImageJ in defined regions that include 150 μm adjacent to the border zone. The percentages of PCNA$^+$n-mKate$^+$/n-mKate$^+$ cells from individual sections were averaged to establish the hepatocyte proliferation index for each animal.

To quantify leukocyte infiltration, sections from *fabp10a:n-mKate* livers were immunostained with anti-RFP and anti-Lcp1 antibodies (see above). Three sections containing the largest injury areas were imaged. The number of Lcp1$^+$ cells was counted manually using ImageJ in defined regions (150 μm x 150 μm) that include the injury area and border zone. Lcp1+ counts in three independent regions per animal were averaged to establish a quantification for each animal.

To quantify collagen deposition, liver sections were immunostained using an anti-Col1a1 antibody and imaged using confocal microscopy. Three sections containing the largest injury areas were imaged. The Col1a1$^+$ area/total liver parenchyma area ratio in three independent regions per animal was averaged to establish a quantification for each animal.

Quantification and Statistical Analysis

Sample sizes were chosen based on previous publications and are indicated in each figure legend. No animal or sample was excluded from the analysis unless the animal died during the procedure. The experiments were not randomized, and the investigators were not blinded to allocation during experiments and outcome assessment. All statistical values are displayed as mean ± standard deviation. The figures or figure legends indicate sample sizes, statistical tests, and P values. Data distribution was determined before using parametric or non-parametric statistical tests. Statistical significance was assigned at $P < 0.05$. All statistical tests were performed using Prism 7 software.

Bulk RNA-seq

Sham and injured livers at 1, 3, and 7 dpci were phenotyped under the fluorescent stereomicroscope (NSZ-606 Binocular Zoom fitted with a NightSea SFA light base) to confirm the presence of insult upon cryoinjury. In addition, 3 adult zebrafish livers were pooled per tube, discriminating between the injured border and liver tissue from other lobes. Finally, 3 replicates of 3 pooled livers were used for library preparation. Livers were transferred to a final volume of 300uL of cold TRIzol™ (Thermo Fisher Scientific) per tube on ice. Livers were homogenized using the mechanical homogenizer for 30s on ice, with a plastic pestle, to ensure fine homogenization. RNA was extracted according to the manufacturer guidelines (Direct-zolT™ RNA MiniPrep kit, Zymo Research). RNA quality was confirmed using an Agilent 4200 Tapestation System. Libraries were sequenced in Illumina NextSeq 500, with paired-end 75bp reads to a depth of 15M reads per sample.

Bioinformatic analysis

BCL files were converted to FastQ files on Galaxy using bcl2fastq2 (v2.20.0.422 – Illumina). Reads were mapped to the reference genome (Ensembl build 11, release 94) using Hisat2, version 2.1.0 (Kim et al., 2015), and counting was performed using featureCounts, version1.6.0 (Liao et al., 2014. For bioinformatics analysis, we compared SHAM, 1, 3 and 7 dpci livers. Downstream analysis was performed in R, version 4.2.2 (R Core Team, 2018). Counts were normalized and differential expression between design groups was tested using the package EdgeR. Principal component analysis (PCA) plots, volcano plots and heatmaps were generated using the ggplot2 package, version 3.4.0 (H. Wickham. ggplot2: Elegant Graphics for DataAnalysis. Springer-Verlag New York, 2016.). For the enrichment, we selected all the Gene Stable IDs, translated them to Mus musculus Gene Stable IDs, and obtained the ENTREZIDs and SYMBOLs using biomaRt package (Durinck et al., 2005). Statistical significant genes were define with the following thresholds, log2FC≥1.5 and p-value ≤0.05. Transcriptional downstream signatures were examined using Gene Set Enrichment Analysis (GSEA v4.0.3) (Subramanian et al., 2005). Gene ontology analysis was done using Gene Ontology Panther (http://geneontology.org).

Abbreviations

AFOG: Fuchsin Orange G
ALF: Acute liver failure
APAP: Acetaminophen (N-acetyl-para-aminophenol
BECs: Biliary epithelial cells
BrdU: 5-Bromo-2 -deoxyuridine
CCl4: Carbon tetrachloride
DAPI: 4′,6-diamidino-2-phenylindole
DDC: 3,5-diethoxycarbonyl-1,4-dihydrocollidine
DEG: Differentially expressed genes
DMN: Dimethyl nitrosamine
Dpci: Days post-cryoinjury
ECM: Extracellular matrix
EC: Endothelial cell
FFPE: Formalin-fixed, paraffin-embedded tissue
GSEA: Gene Set Enrichment analysis
HCC: Hepatocellular carcinoma
HPx: Hepatectomy
HSCs: Hepatic Stellate cells
IA: Injured area
LSEC: Liver Sinusiodal Endothelial Cell
Mpci: Months post-cryoinjury
NES: Normalised enrichment score
NTR: Nitroreductase
PCNA: Proliferating cell nuclear antigen
PFA: Paraformaldehyde
TAA: ThioacetamideYpci: years post-cryoinjury
Ypci: Years post-cryoinjury

Acknowledgements

M.S.-M. is supported by the Early.Postdoc Mobility fellowship from the Swiss National Science Foundation (SNSF).
D.B received support from the Wallonie Bruselles International Postdoctoral Fellowship.
J.M.G.-R. is supported by the National Institutes of Health (1R01HL164749-01), the American Heart Association (19CDA34660207), the Corrigan Minehan Foundation (SPARK Award), and the Hassenfeld Foundation (Hassenfeld Research Scholar Award).
A.G.C is supported by an NHMRC Investigator Grant (GNT1176650), and an ARC Discovery Project Grant (DP200102693).
We also extend our thanks to the Peter MacCallum Cancer Centre Core Facilities and their staff who supported this work; namely the Centre for Advanced Histology & Microscopy, the Molecular Genomics Core and Bioinformatics Core Facilities. We also thank the staff involved at the University of Melbourne Zebrafish Core Facility (DRUM) and BOMP (Biology Optical Microscopy Platform). Finally, we thank members of the Cox Laboratory (Peter MacCallum Cancer Centre) González-Rosa Laboratory and the Organogenesis and Cancer program at Peter MacCallum Cancer Centre for helpful discussions.

Supplementary Figures

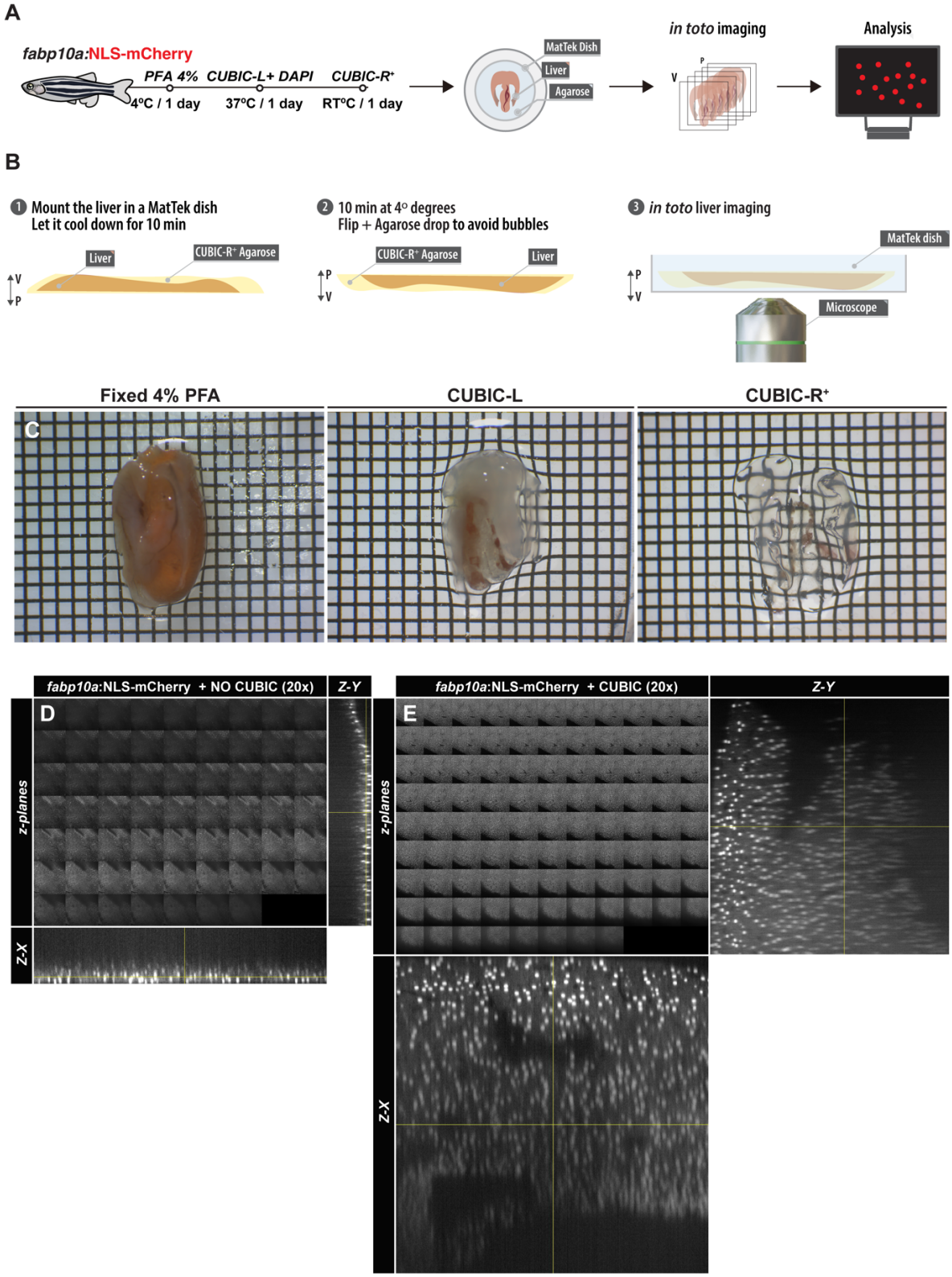

Supplementary Figure 1. CUBIC-clearing liver method. A) Schematic representation of the liver CUBIC-clearing procedure for imaging the liver. B) Mounting strategy for imaging cleared livers. Livers are embedded in CUBIC-agarose within a MatTek dish, positioning the IA facing-up. The CUBIC-agarose disc containing embedded livers is cooled down for 10 minutes at 4 degrees Celsius. Once the CUBIC-agarose disc solidifies, it is carefully flipped using forceps, and a drop of CUBIC-agarose is

added to prevent bubble formation. Cleared livers are prepared for imaging from this point onwards. C) An example of the liver-clearing process during the CUBIC-clearing procedure. D-E) z-stack representative examples, with Z-X and Z-Y projections, of non-cleared (D) and CUBIC-cleared (E) in toto liver confocal acquisitions.

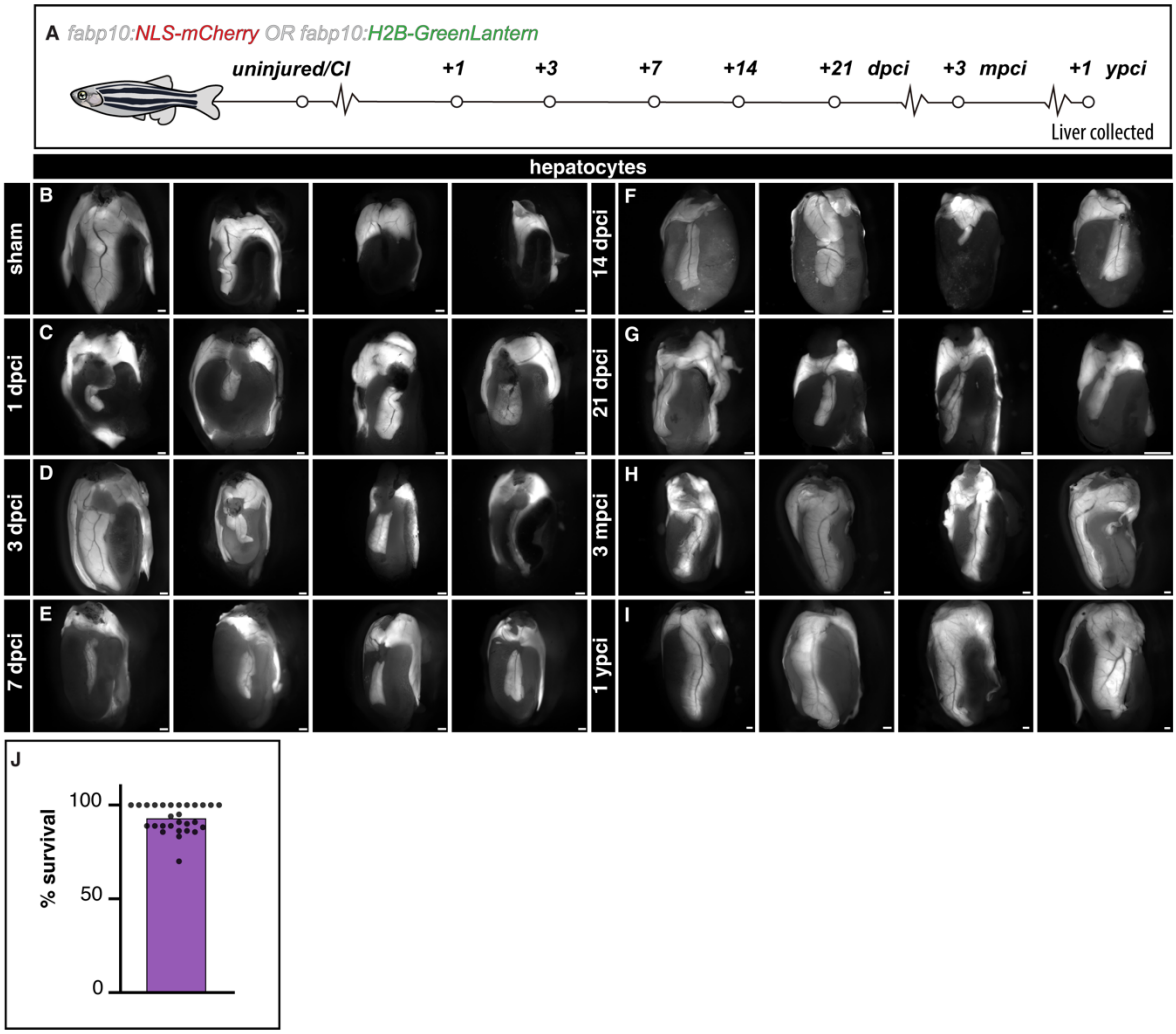

Supplementary Figure 2. Temporal dynamics of liver regeneration in zebrafish following cryoinjury. A) Schematic representation of the timing of sample collection following cryoinjury. B-I) Epifluorescence acquisitions of adult zebrafish Tg(*fabp10a: GreenLantern-H2B*) or Tg(*fabp10a:NLS-mCherry*) livers at different stages of regeneration upon cryoinjury. J) Zebrafish survival upon cryoinjury. Scale bars: 500 μm.

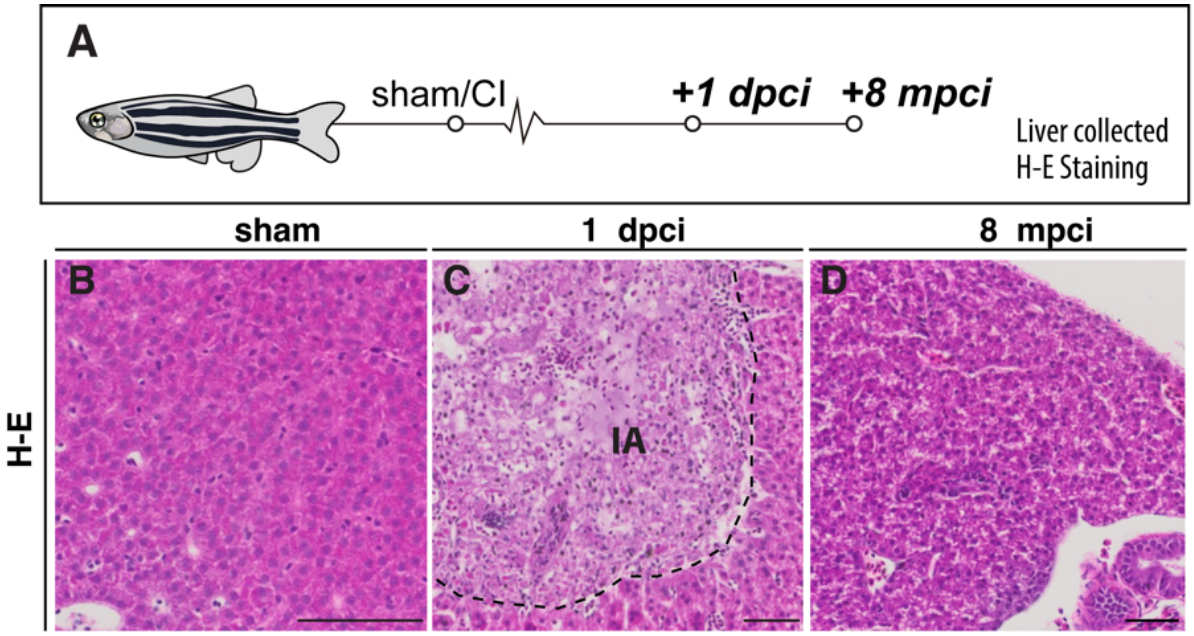

Supplementary Figure 3. Histological appearance of regenerating livers following cryoinjury. A) Schematic representation of the timing of sample collection following cryoinjury for histological examination. Anterior is towards the left, dorsal is towards the top (B and D). Anterior is ventral and posterior is dorsal (C). B) H&E staining of sham adult zebrafish liver. C) H&E staining of 1 dpci adult zebrafish. D) H&E staining of regenerated adult zebrafish liver at 8 months post-cryoinjury (mpci) Scale bars: 50 μm.

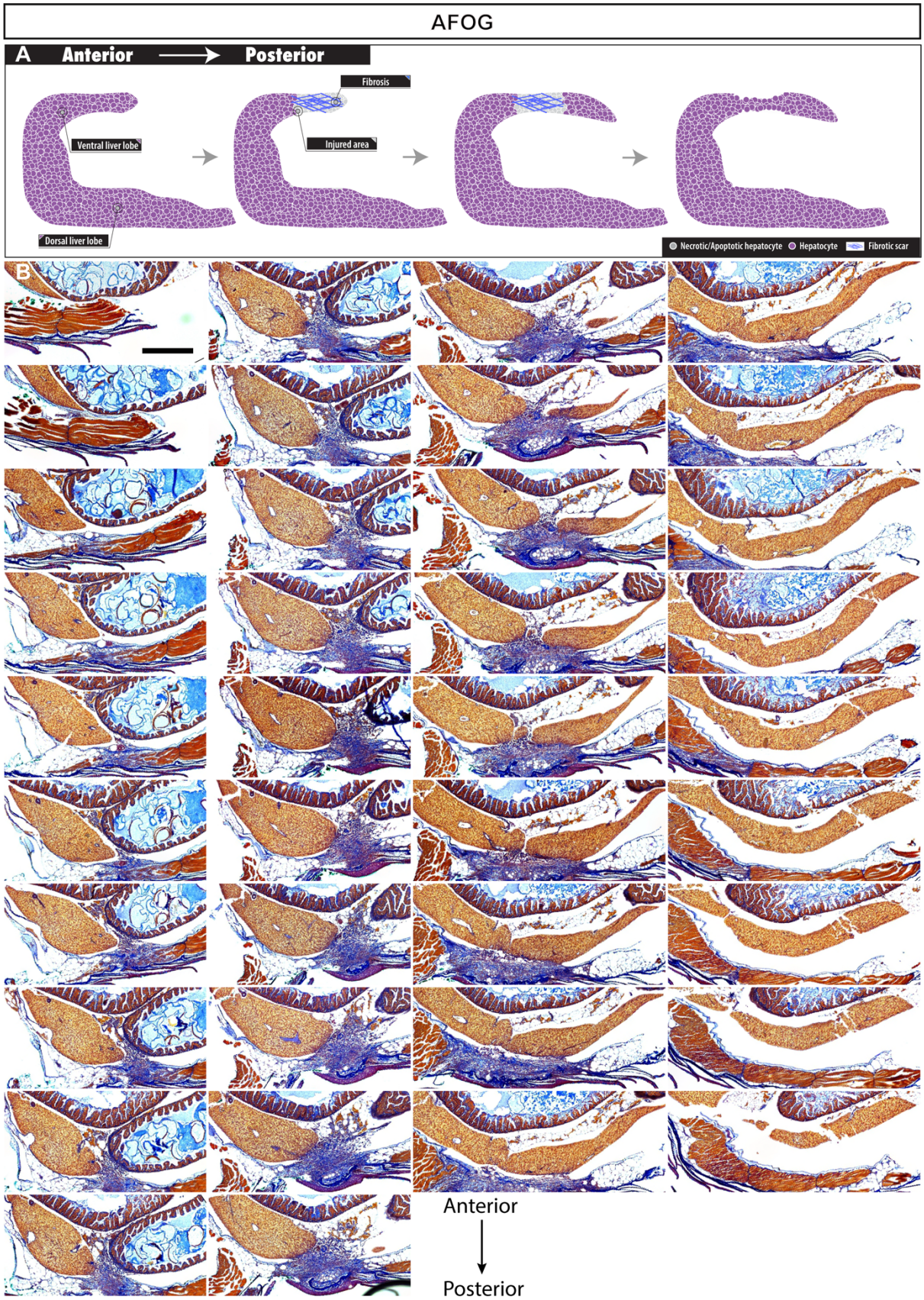

Supplementary Figure 4. AFOG staining of 5 dpci liver. B) Schematic representation of the histology section plane across 5 dpci adult zebrafish liver. B) AFOG staining of consecutive sections of 5 dpci adult zebrafish liver. Blue: collagen; Red: cell debris and fibrin. Anterior is towards the left, dorsal is towards the top. Scale bars: 500 μm.

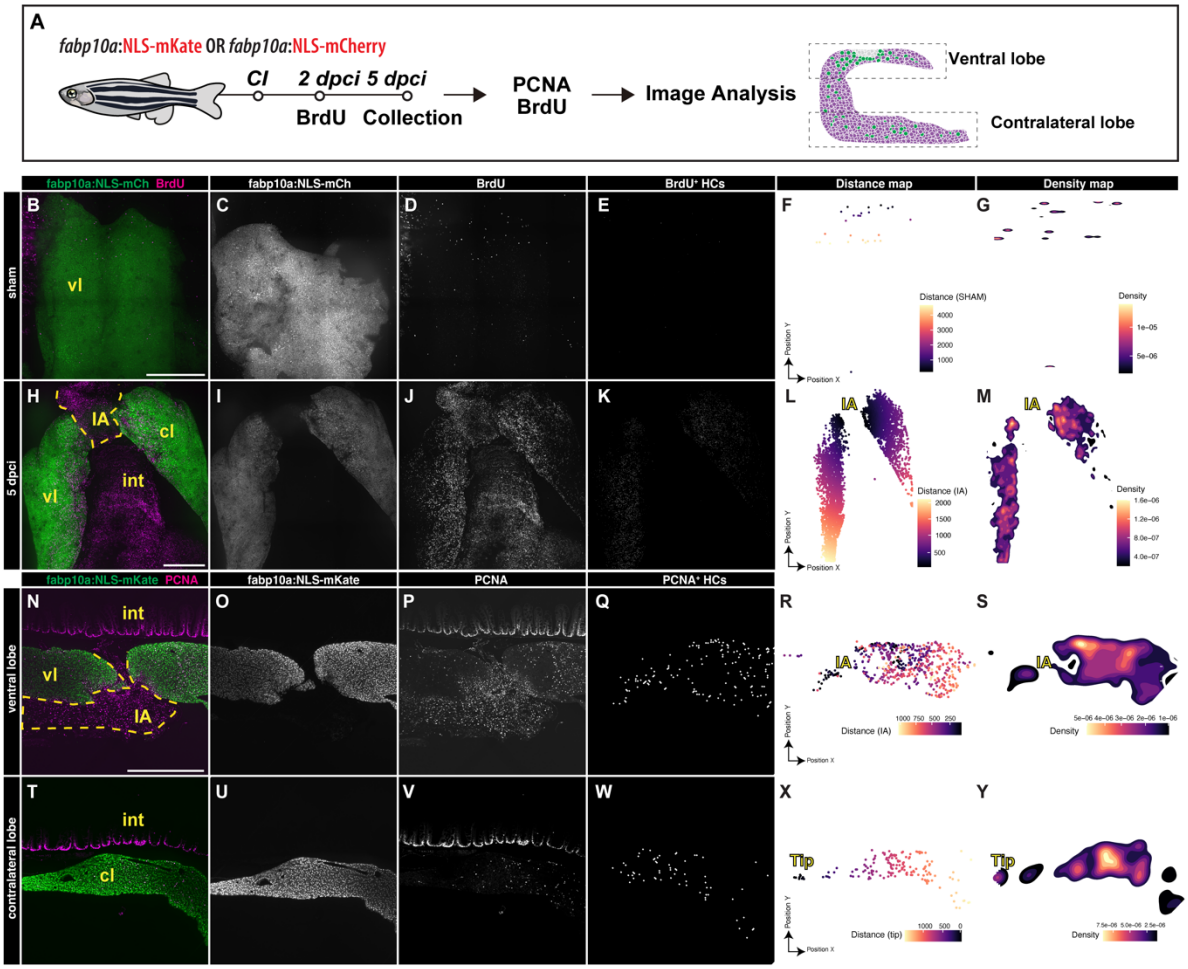

Supplementary Figure 5. Cryoinjury induces local and distal compensatory hyperplasia. A) Schematic representation of the timing of sample collection following cryroinjury for BrdU and PCNA analysis. B-E) *in toto* of BrdU-pulse labelling sham adult zebrafish confocal acquisition. F) *in toto* confocal acquisition segmentation of BrdU+/mCherry+ hepatocyte nuclei position towards the rostral area of the liver in sham livers. Colour scale represents the calculation of distance of every nuclei respect to rostral part of the liver. G) *in toto* confocal acquisition segmentation of BrdU+/mCherry+ hepatocyte nuclei and density analysis using a Kernel Density Estimation (KDE) algorithm presented as a corresponding heatmap and quantification of the proliferating hepatocyte density in sham animals. H-K) *in toto* of BrdU-pulse labelling 5 dpci adult zebrafish confocal acquisition. L) *in toto* confocal acquisition segmentation of BrdU+/mCherry+ hepatocyte nuclei position towards the IA in 5 dpci livers. Colour scale represents the calculation of distance of every nuclei respect to IA. M) *in toto* confocal acquisition segmentation of BrdU+/mCherry+ hepatocyte nuclei and density analysis using a Kernel Density Estimation (KDE) algorithm presented as a corresponding heatmap and quantification of the proliferating hepatocyte density from the injured area, N-Q) Confocal acquisition of 5 dpci ventral lobe liver sections. R) Section confocal acquisition segmentation of PCNA+/mKate+ hepatocyte nuclei position towards the IA in injured livers. Colour scale represents the calculation of distance of every nuclei respect to the IA. S) Section confocal acquisition segmentation PCNA+/mKate+ hepatocyte nuclei and density analysis using a Kernel Density Estimation (KDE) algorithm presented as a corresponding heatmap and quantification of the proliferating hepatocyte density from the injured area in the ventral lobe. T-W) Confocal acquisition of 5 dpci contralateral lobe liver sections. X) Section confocal acquisition segmentation of PCNA+/mKate+ hepatocyte nuclei position towards the tip of the contralateral lobe in sham livers. Colour scale represents the calculation of distance of every nuclei respect to the tip. Y) Section confocal acquisition segmentation of PCNA+/mKate+ hepatocyte nuclei and density analysis using a Kernel Density Estimation (KDE) algorithm presented as a corresponding heatmap and quantification of the proliferating hepatocyte density from the tip of the contralateral lobe. cl: contralateral lobe; Dashed line: Border zone of the injured area; IA: injured area; int: intestine; vl: ventral lobe. Scale bars: 500 μm.

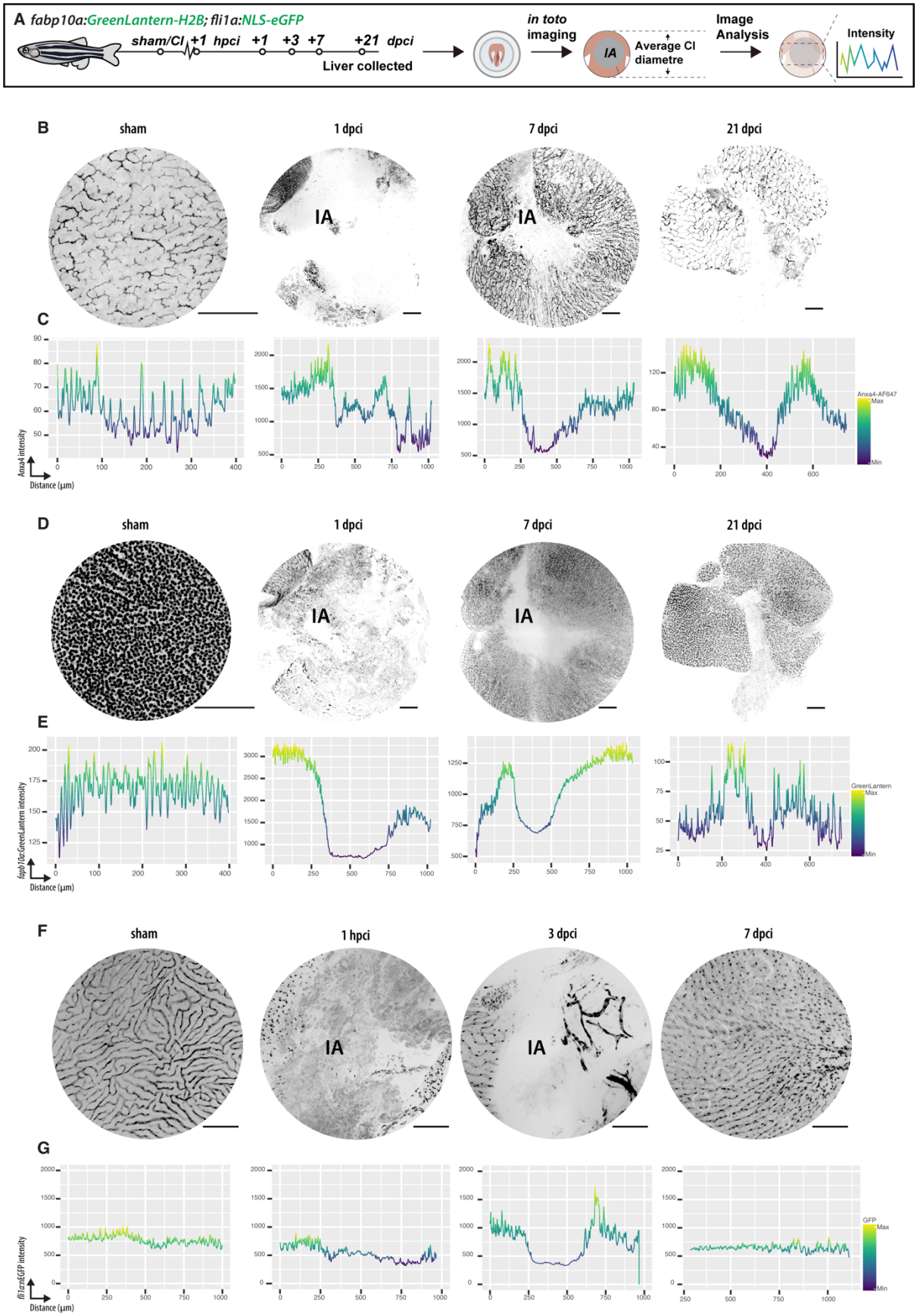

Supplementary Figure 6. Regeneration of the injured area. A) Schematic workflow from data acquisition to image analysis. B) Region of interest (ROI) representing the average injured area size of Anxa4 staining in adult livers inverted confocal acquisitions. C) Anxa4's pixel distribution alongside the injured area throughout different regeneration stages. D) ROI representing the average injured area

size of Tg(*fabp10a:GreenLantern-H2B*) adult livers inverted confocal acquisitions. E) GreenLantern's pixel distribution alongside the injured area throughout different regeneration stages. F) ROI representing the average injured area size of Tg(*fli1a:NLS-eGFP*) adult livers inverted confocal acquisitions. G) GFP's pixel distribution alongside the injured area throughout different regeneration stages. Scale bars: 125 *µ*m.

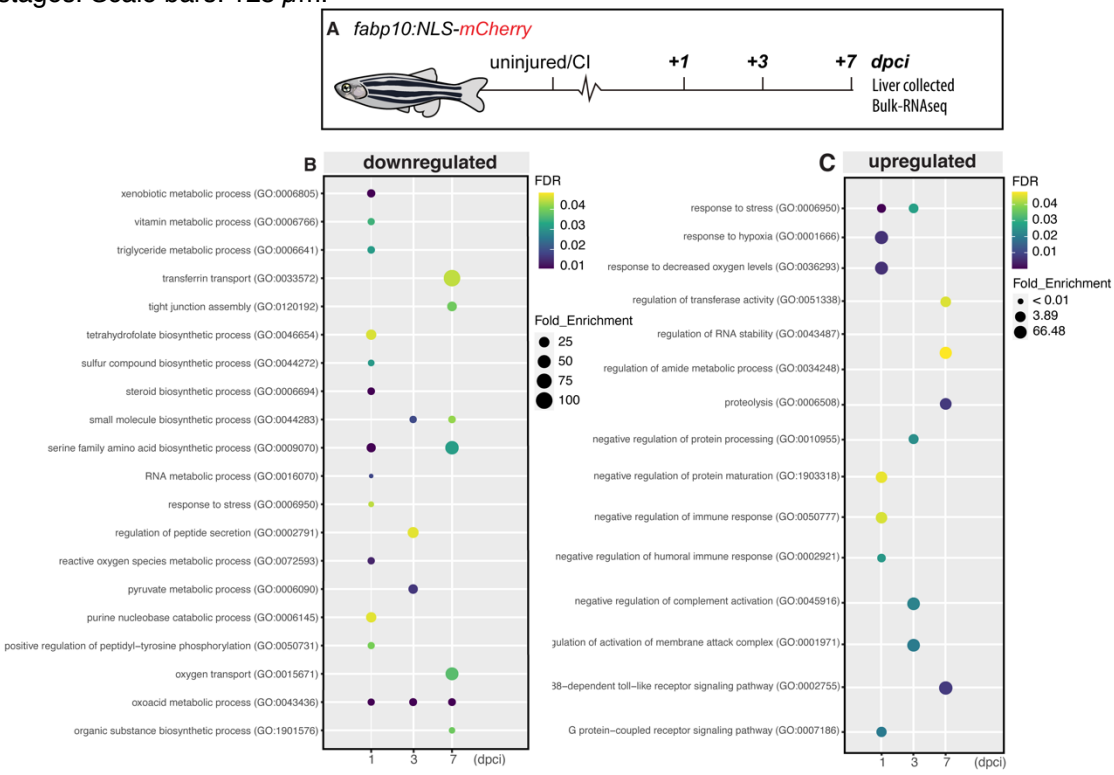

Supplementary Figure 7. Comprehensive Gene Ontology (GO) Analysis of Regenerating Liver Tissue. A) Graphical illustration of the collection process for liver stages following cryoinjury. B) Enriched gene ontology terms for DEG in downregulated genes through from sham to 7 dpci. C) Enriched gene ontology terms for DEG in upregulated genes through from sham to 7 dpci.

	Cryoinjury	HPx	Genetic ablation	APAP
Tissue affected	Parenchymal and non-parenchymal cells	Apoptosis limited to the tissue around the amputation site	Promoter-specific ablation (Only hepatocytes)	Pericentral hepatocytes and surronding parenchymal and non-parenchymal cells
Regeneration	30	5-7	5	5-7
Fibrosis	Yes	No	No	No
Localised injury response	Yes	No	No	No
Regeneration response	Local hyperplasia & Compensatory growth	Compensatory growth	BECs Transdifferentiation	Compensatory hyperplasia
Inflammation	Major	Major	Major	Minor
Specific transgene	No	No	Yes	Yes

Table 1. Comparison of liver injury and regeneration methods in animal models.

1. Michalopoulos, G. K. & Bhushan, B. Liver regeneration: biological and pathological mechanisms and implications. *Nat Rev Gastroenterol Hepatol* **18**, 40–55 (2021).
2. Pellicoro, A., Ramachandran, P., Iredale, J. P. & Fallowfield, J. A. Liver fibrosis and repair: immune regulation of wound healing in a solid organ. *Nature Reviews Immunology 2014 14:3* **14**, 181–194 (2014).
3. González-Rosa, J. M., Martín, V., Peralta, M., Torres, M. & Mercader, N. Extensive scar formation and regression during heart regeneration after cryoinjury in zebrafish. *Development* **138**, 1663–1674 (2011).
4. Schnabel, K., Wu, C. C., Kurth, T. & Weidinger, G. Regeneration of cryoinjury induced necrotic heart lesions in zebrafish is associated with epicardial activation and cardiomyocyte proliferation. *PLoS One* **6**, (2011).
5. Chablais, F., Veit, J., Rainer, G. & Jawiska, A. The zebrafish heart regenerates after cryoinjury-induced myocardial infarction. *BMC Dev Biol* **11**, (2011).
6. Mitchell, C. & Willenbring, H. A reproducible and well-tolerated method for 2/3 partial hepatectomy in mice. *Nat Protoc* **3**, 1167–1170 (2008).
7. Kan, N. G., Junghans, D., Carlos, J. & Belmonte, I. Compensatory growth mechanisms regulated by BMP and FGF signaling mediate liver regeneration in zebrafish after partial hepatectomy. *The FASEB Journal* **23**, 3516–3525 (2009).
8. Sadler, K. C., Krahn, K. N., Gaur, N. A. & Ukomadu, C. Liver growth in the embryo and during liver regeneration in zebrafish requires the cell cycle regulator, uhrf1. *Proc Natl Acad Sci U S A* **104**, 1570–1575 (2007).
9. Constandinou, C., Henderson, N. & Iredale, J. P. Modeling liver fibrosis in rodents. *Methods Mol Med* **117**, 237–250 (2005).
10. RUBIN, E., HUTTERER, F. & POPPER, H. Cell Proliferation and Fiber Formation in Chronic Carbon Tetrachloride Intoxication: A Morphologic and Chemical Study. *Am J Pathol* **42**, 715 (1963).
11. Iredale, J. P. *et al.* Tissue inhibitor of metalloproteinase-1 messenger RNA expression is enhanced relative to interstitial collagenase messenger RNA in experimental liver injury and fibrosis. *Hepatology* **24**, 176–184 (1996).
12. Ala-Kokko, L., Pihlajaniemi, T., Myers, J. C., Kivirikko, K. I. & Savolainen, E. R. Gene expression of type I, III and IV collagens in hepatic fibrosis induced by dimethylnitrosamine in the rat. *Biochemical Journal* **244**, 75 (1987).
13. Kitamura, K. *et al.* Pathogenic roles of tumor necrosis factor receptor p55-mediated signals in dimethylnitrosamine-induced murine liver fibrosis. *Lab Invest* **82**, 571–583 (2002).
14. Yoshida, T. *et al.* SOCS1 Is a Suppressor of Liver Fibrosis and Hepatitis-induced Carcinogenesis. *J Exp Med* **199**, 1701 (2004).
15. Müller, A., Machnik, F., Zimmermann, T. & Schubert, H. Thioacetamide-induced cirrhosis-like liver lesions in rats--usefulness and reliability of this animal model. *Exp Pathol* **34**, 229–236 (1988).
16. Salguero Palacios, R. *et al.* Activation of hepatic stellate cells is associated with cytokine expression in thioacetamide-induced hepatic fibrosis in mice. *Lab Invest* **88**, 1192–1203 (2008).
17. Ding, Z. & Zhuo, L. Attenuation of hepatic fibrosis by an imidazolium salt in thioacetamide-induced mouse model. *J Gastroenterol Hepatol* **28**, 188–201 (2013).
18. Fickert, P. *et al.* A New Xenobiotic-Induced Mouse Model of Sclerosing Cholangitis and Biliary Fibrosis. *Am J Pathol* **171**, 525 (2007).
19. Mossanen, jc & Tacke, f. Acetaminophen-induced acute liver injury in mice. *Lab Anim* **49**, 30–36 (2015).

20. Bhushan, B. *et al.* Pro-Regenerative Signaling after Acetaminophen-Induced Acute Liver Injury in Mice Identified Using a Novel Incremental Dose Model. *Am J Pathol* **184**, 3013–3025 (2014).
21. Bhushan, B. & Apte, U. Liver Regeneration after Acetaminophen Hepatotoxicity: Mechanisms and Therapeutic Opportunities. *Am J Pathol* **189**, 719 (2019).
22. North, T. E. *et al.* PGE2-regulated wnt signaling and N-acetylcysteine are synergistically hepatoprotective in zebrafish acetaminophen injury. *Proc Natl Acad Sci U S A* **107**, 17315–17320 (2010).
23. Passeri, M. J., Cinaroglu, A., Gao, C. & Sadler, K. C. Hepatic steatosis in response to acute alcohol exposure in zebrafish requires sterol regulatory element binding protein activation. *Hepatology* **49**, 443–452 (2009).
24. Popper, H. & Leiber, C. S. Histogenesis of alcoholic fibrosis and cirrhosis in the baboon. *Am J Pathol* **98**, 695 (1980).
25. Tsukamoto, H., Towner, S. J., Clofalo, L. M. & French, S. W. Ethanol-induced liver fibrosis in rats fed high fat diet. *Hepatology* **6**, 814–822 (1986).
26. Cordero-Espinoza, L. & Huch, M. The balancing act of the liver: tissue regeneration versus fibrosis. *Journal of Clinical Investigation* **128**, 85–96 (2018).
27. Sun, T. *et al.* AXIN2+ Pericentral Hepatocytes Have Limited Contributions to Liver Homeostasis and Regeneration. *Cell Stem Cell* **26**, 97-107.e6 (2020).
28. Curado, S., Stainier, D. Y. R. & Anderson, R. M. Nitroreductase-mediated cell/tissue ablation in zebrafish: a spatially and temporally controlled ablation method with applications in developmental and regeneration studies. *Nat Protoc* **3**, 948–954 (2008).
29. Benmoshe, S. *et al.* The spatiotemporal program of zonal liver regeneration following acute injury. *Stem Cell* **29**, 973-989.e10 (2022).
30. Mikami, S. ichi, Kurosu, T. & Farner, D. S. Light- and electron-microscopic studies on the secretory cytology of the adenohypophysis of the Japanese quail, Coturnix coturnix japonica. *Cell Tissue Res* **159**, 147–165 (1975).
31. Wang, C. *et al.* Macrophage Polarization and Its Role in Liver Disease. *Front Immunol* **12**, 5381 (2021).
32. Heinke, P. *et al.* Diploid hepatocytes drive physiological liver renewal in adult humans. *Cell Syst* **13**, 499-507.e12 (2022).
33. VanSaun, M. N., Mendonsa, A. M. & Lee Gorden, D. Hepatocellular Proliferation Correlates with Inflammatory Cell and Cytokine Changes in a Murine Model of Nonalchoholic Fatty Liver Disease. *PLoS One* **8**, e73054 (2013).
34. Arrojo e Drigo, R. *et al.* Age Mosaicism across Multiple Scales in Adult Tissues. *Cell Metab* **30**, 343-351.e3 (2019).
35. Michalopoulos, G. K. & DeFrances, M. C. Liver regeneration. *Science (1979)* **276**, 60–65 (1997).
36. Weng, H. *et al.* Two sides of one coin: Massive hepatic necrosis and progenitor cell-mediated regeneration in acute liver failure. *Front Physiol* **6**, (2015).
37. Yanger, K. *et al.* Adult hepatocytes are generated by self-duplication rather than stem cell differentiation. *Cell Stem Cell* **15**, 340–349 (2014).
38. Kramann, R. *et al.* Perivascular Gli1+ Progenitors Are Key Contributors to Injury-Induced Organ Fibrosis. *Cell Stem Cell* **16**, 51–66 (2015).
39. Shin, S., Upadhyay, N., Greenbaum, L. E. & Kaestner, K. H. Ablation of Foxl1-Cre–Labeled Hepatic Progenitor Cells and Their Descendants Impairs Recovery of Mice From Liver Injury. *Gastroenterology* **148**, 192-202.e3 (2015).
40. McKenna, A. *et al.* Whole-organism lineage tracing by combinatorial and cumulative genome editing. *Science (1979)* **353**, (2016).

41. Raj, B. *et al.* Simultaneous single-cell profiling of lineages and cell types in the vertebrate brain. *Nat Biotechnol* **36**, 442–450 (2018).
42. Kong, W. *et al.* CellTagging: combinatorial indexing to simultaneously map lineage and identity at single-cell resolution. *Nat Protoc* **15**, 750–772 (2020).
43. Morris, S. A. The evolving concept of cell identity in the single cell era. *Development (Cambridge)* **146**, 1–5 (2019).
44. Bowling, S. *et al.* An Engineered CRISPR-Cas9 Mouse Line for Simultaneous Readout of Lineage Histories and Gene Expression Profiles in Single Cells. *Cell* **181**, 1410-1422.e27 (2020).
45. Rao, A., Barkley, D., França, G. S. & Yanai, I. Exploring tissue architecture using spatial transcriptomics. *Nature 2021 596:7871* **596**, 211–220 (2021).
46. Moffitt, J. R., Lundberg, E. & Heyn, H. The emerging landscape of spatial profiling technologies. *Nature Reviews Genetics 2022 23:12* **23**, 741–759 (2022).
47. Sande-Melón, M. *et al.* Adult sox10+ Cardiomyocytes Contribute to Myocardial Regeneration in the Zebrafish. *Cell Rep* **29**, 1041-1054.e5 (2019).
48. Matsumoto, K. *et al.* Advanced CUBIC tissue clearing for whole-organ cell profiling. *Nat Protoc* **14**, 3506–3537 (2019).
49. Schindelin, J. *et al.* Fiji: An open-source platform for biological-image analysis. *Nature Methods* vol. 9 676–682 Preprint at https://doi.org/10.1038/nmeth.2019 (2012).
50. Koth, J. *et al.* Runx1 promotes scar deposition and inhibits myocardial proliferation and survival during zebrafish heart regeneration. *Development (Cambridge)* **147**, (2020).